

Interface dynamics and banding in rapid solidification

Alain Karma and Armand Sarkissian

Physics Department, Northeastern University, Boston, Massachusetts 02115

(Received 29 July 1992)

Rapid-solidification experiments on metallic alloys in the last decade have provided widespread observations of a novel “banded structure.” We report the results of numerical and analytical studies of the interface dynamics underlying the formation of this structure in a model of directional solidification which includes both solute and heat diffusion and nonequilibrium effects. The thrust of these studies is on the unsteady dynamics of the planar interface and thermal effects. The main conclusion is that the origin of banding can be related to relaxation oscillations of the solidification front, characterized by large variations of the interface velocity, which are dramatically affected by latent-heat diffusion. Without the latter, the oscillations are found to be reasonably well approximated by the phenomenological model of Carrard *et al.* [Acta Metall. **40**, 983 (1992)], and the band spacing is inversely proportional to the temperature gradient. In contrast, with latent-heat diffusion the band spacing is insensitive to the temperature gradient, but is controlled instead by the interplay of solute and heat diffusion. The smallness of the solutal diffusivity to thermal diffusivity ratio is exploited to explain analytically this effect and to derive considerably simpler equations of interface motion that provide an efficient numerical means to study the nonplanar interface dynamics expected to cause dark bands. A reasonable agreement with experiment is found for the spacing of banded structures dominated by light-band microsegregation-free regions in Al-Fe alloys.

PACS number(s): 61.50.Cj, 05.70.Ln, 64.70.Dv, 81.30.Fb

I. INTRODUCTION

During the last decade, a major research effort has been aimed at developing a fundamental understanding of a wide range of interfacial pattern formation phenomena in crystal growth [1–3]. So far, the classic dendritic, cellular, and lamellar eutectic microstructures studied experimentally in transparent organic materials and metallic alloys under *slow-solidification* conditions (with growth rates $\sim \mu\text{m}/\text{sec}$) have been the primary focus of theoretical investigation. More recently, there has been a growing interest in characterizing the microstructure of alloys, which, in contrast, are produced under *rapid-solidification* (RS) conditions (with growth rates $\sim \text{cm}/\text{sec}$ – m/s) by a variety of techniques ranging from laser or electron-beam surface remelting, melt spinning, and atomization [3].

Perhaps one of the most surprising observations that has come out of RS experiments, from a microstructural standpoint, is that of the so-called “banded structure” composed of alternating light and dark bands lying parallel to the solidification front (Fig. 1). First observed as an isolated phenomenon about one decade ago [4], this structure has since then been found to be a common microstructural characteristic of many alloys solidified under growth conditions that approach absolute stability [5]. Moreover, detailed experimental studies in Ag-Cu [6], Al-Cu [7], and Al-Fe [8] have shown that the dark bands have a precipitate structure, either cellular-dendritic or eutectic, depending on the alloy composition, which is similar to the precipitate structure observed at lower growth rate preceding the appearance of the banded structure. In contrast, the light bands have

a microsegregation-free structure similar to the one observed at larger growth rate following the disappearance of the banded structure. Also, although typically observed to be nearly regular, the banded structure has occasionally been found to be highly irregular [8], or observed, in transverse sections, to form a spiral-shape “swirling structure” [9] with a wavelength equal to the band spacing.

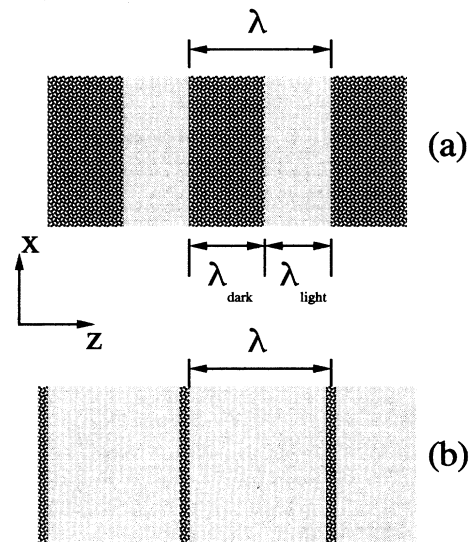


FIG. 1. Schematic drawing of the banded structure. The z and x axes are respectively parallel to the growth direction and to the solidification front.

According to the classic Mullins-Sekerka (MS) linear stability analysis of the planar interface [10], one would have expected a cellular-array structure to form, at velocities just below the absolute stability limit, V_{AS} , beyond which the planar interface is completely stable, and a planar interface leading to a microsegregation-free structure at velocities above V_{AS} . This type of scenario has actually been observed in sufficiently dilute Ag-Cu alloys by Boettinger *et al.* [6], but at larger compositions of Cu it is the banded structure that was observed instead, comprised for a range of growth rate between cellular and microsegregation-free solidification. In several other alloys such as Al-Fe the banded structure persists at even more dilute alloy compositions [8].

An important clue as to why the MS analysis fails to signal the appearance of banding was provided by Coriell and Sekerka (CS), who redid the analysis incorporating nonequilibrium effects to account for the fact that the assumption of local thermodynamic equilibrium at the interface breaks down at large solidification rate [11]. In particular, they introduced a velocity-dependent segregation coefficient $k(v)$ and identified a novel instability, driven by solute trapping, with a new absolute stability limit V_{AS} that is comparable in magnitude but larger than the old absolute stability limit of the MS analysis.

As CS showed, this instability is a longwavelength oscillatory instability that should lead, for velocities slightly less than V_{AS} , to transverse (perpendicular to the growth direction) cellularlike spatial inhomogeneities of concentration with periodic variations in time. These inhomogeneities—although probably occurring but not visualizable in micrographs because they are not sufficiently large to cause the precipitation of a “dark” impurity reach phase—do not account directly for the banded structure, which, in contrast, is characterized by an alternation of structure along the growth direction. However, for velocities below a second threshold V_c less than V_{AS} , the zero wave number (planar part) of the CS stability spectrum becomes unstable, together with other, already unstable, finite-wave-number instabilities. It is this planar instability that is most relevant to banding and, as was found recently [12], triggers relaxation oscillations of the solidification front.

The conjecture that a planar instability could set up relaxation oscillations that would account for banding was proposed earlier by Merchant and Davis [13] in the context of a linear stability analysis of a closely related model of rapid solidification, which is based on the so-called “frozen-temperature approximation” (FTA). In this approximation, latent-heat diffusion (LHD) is neglected and the temperature field is approximated by a moving temperature gradient. The planar instability of this model has the same physical origin (solute trapping) as the CS instability, which, as a consequence of the FTA, becomes shifted to zero wave number at V_{AS} . Recent analytical [14] and numerical studies [15] of the same model have also found relaxation oscillations. However, generically, these are dramatically altered by LHD [12] and, for this reason, cannot be used as a basis for a quantitative characterization of banding.

Recently, Carrard, Gremaud, Zimmermann, and Kurz

(CGZK) [8, 16] have proposed a phenomenological model of banding, based on periodic instabilities of the growth velocity. In this model, cyclic interface motion occurs between two stable (cellular-dendritic and planar) branches of an S-shaped $T(V)$ curve corresponding to the temperature of the steady-state solidification front. This cyclic motion occurs whenever the isotherm velocity V_0 drives the solidification front at a velocity that falls on a middle unstable branch of the $T(V)$ curve. The instability of this branch is directly related to the aforementioned planar instability. This model has two main advantages. Firstly, it accounts for the formation of alternate dark (left branch) and light bands (right branch). Secondly, it allows one to make quantitative predictions of the light and dark band spacings λ_{light} and λ_{dark} (and the total band spacing $\lambda = \lambda_{\text{light}} + \lambda_{\text{dark}}$). However, this model has two limitations. Firstly, it is mainly phenomenological and thus it needs to be examined further to determine if it actually describes the dynamical behavior of the underlying equations of interface motion; and, secondly, it relies on the FTA.

A similar idea of explaining banding in terms of a cyclic interface motion was proposed previously by Aziz [17]. In contrast to the CGZK model, his explanation was based on cycles in the temperature-concentration (T - X) plane that should occur when a tie line connects a kinetic solidus with a kinetic liquidus having opposite slopes. There is the interesting possibility that such cycles could also yield bands. However, it should be noted that such an explanation does not apply to dilute alloy compositions where bands are also observed.

The primary goal of the present paper is to investigate the nature of the dynamical mechanism underlying the formation of the banded structure. It has been geared towards providing at least partial answers to the following questions:

- (1) Does the planar instability actually lead in a nonlinear regime to time-periodic changes in velocity that can account for the formation of bands?
- (2) To what extent are these changes described by the CGZK model?
- (3) What is the role of LHD?
- (4) What are the dominant physical factors that control the band spacing?

A brief summary of our results has been published earlier [12], and we give here a more detailed exposition that includes additional results and new analyses. The outline of the paper is as follows. In Sec. II, we write down the basic equations of the model and briefly discuss some of its limitations. This model is essentially an extension of the one-sided model of the directional solidification [18], which includes LHD and the same nonequilibrium effects considered in the CGZK model and in Refs. [13], [14], and [15]. These corrections include a velocity-dependent segregation coefficient following a model of Aziz and Kaplan [19], the effect of attachment kinetics, and a velocity-dependent liquidus following a thermodynamically consistent model derived by Boettinger and Coriell [20].

Next, we provide in Sec. III a linear stability analysis of the model and present results for Al-Fe and Al-Cu alloys. The purpose of this analysis is essentially to pin-

point more precisely the role of LHD and to determine the neutral stability boundary of the planar instability. The latter determines regions of the composition-velocity plane where banding should occur.

In Sec. IV, we recast the equations of interface motion in a boundary integral form, which serves as a basis for the numerics and for the small solute to thermal diffusivity ratio (Lewis number) analysis presented in Sec. V. There, we derive a “reduced-temperature equation” (RTE), which is used in Sec. VI to understand analytically the effect of LHD and is shown to lead to considerably more efficient numerics, both in one and two dimensions.

Next, in Sec. VI, we investigate numerically the dynamics of the planar interface and its implications for banding. Details of the numerics are presented and the numerical advantage of the RTE in both one dimension (1D) and 2D is discussed. Cycles computed using the FTA are then compared to the cycles predicted by the CGZK model. The role of LHD is then explored by studying how the cyclic motion of the interface becomes modified by its inclusion. A simple analytical theory that explains why this role is quantitatively important is presented. The cycles calculated with LHD are then used together with earlier results of linear stability to interpret the banded structure. Finally, conclusions are given in Sec. VII.

II. BASIC EQUATIONS

Most theoretical investigations to date of *slow* directional solidification have been conducted in the so-called one-sided model in which impurity diffusion in the solid phase is neglected. This model is usually used in conjunction with the aforementioned FTA for the thermal field,

$$T = G(z - V_0 t),$$

which neglects LHD. This approximation is accurate at a small growth rate since the heat flux generated by latent heat at the moving interface is much smaller than the heat flux generated by the externally imposed temperature gradient. However, as will be explained later, latent heat turns out to play a crucial role in banding and, for simplicity, we incorporate its effect here using a symmetric model for the temperature field in which the thermal conductivities are taken to be equal in the solid and liquid phases. The basic equations of interface motion then consist of the usual diffusion equations, in a frame moving with the isotherm velocity V_0 , and the conservation of impurity and heat at the interface:

$$\frac{\partial C}{\partial t} = V_0 \frac{\partial C}{\partial z} + D_C \nabla^2 C, \quad (1)$$

$$\frac{\partial T}{\partial t} = V_0 \frac{\partial T}{\partial z} + D_T \nabla^2 T, \quad (2)$$

$$C_L (1 - k) v_n = -D_C \left[\frac{\partial C}{\partial n} \right]_L, \quad (3)$$

$$L v_n = -c_p D_T \left(\left[\frac{\partial T}{\partial n} \right]_L - \left[\frac{\partial T}{\partial n} \right]_S \right), \quad (4)$$

together with the Gibbs-Thomson condition at the interface modified to include nonequilibrium corrections

$$T_i = T_M + m C_L - \Gamma \kappa - \frac{R T_M^2}{L} \frac{v}{v^*}. \quad (5)$$

The last term on the right-hand side (RHS) of Eq. (5) represents the effect of attachment kinetics where v^* is a kinetic parameter on the order of the velocity of sound in metals. This term is usually negligible under slow solidification conditions but becomes significant at velocities of the order of m/s. Here, D_C and D_T denote, respectively, the solutal and thermal diffusivities, c_p the specific heat at constant pressure, L the latent heat of fusion, T_M the temperature of melting, and Γ the surface tension.

There are two other related nonequilibrium corrections that we take into account in the present model. The first is the effect of solute trapping, which we incorporate using the form derived by Aziz and Kaplan [19], and Jackson, Gilmer, and Leamy [22], and investigated experimentally by Aziz *et al.* [21]:

$$k = \frac{k_e + v_n/v_d}{1 + v_n/v_d}, \quad (6)$$

where v_d is a kinetic parameter. It reflects the fact that, as the interface advances more rapidly, it tends to trap more impurities into the solid phase, thereby leading to a value of the segregation coefficient k larger than its equilibrium value k_e . This velocity-dependent form of k affects the conservation of impurity condition (3). The second is a velocity-dependent form of the liquidus slope m entering Eq. (5):

$$m = m_e \left[1 + \frac{k_e - k(1 - \ln k/k_e)}{1 - k_e} \right], \quad (7)$$

which follows from the thermodynamically consistent interface condition developed by Boettinger and Coriell [20] based on an earlier model of Baker and Cahn [23].

Finally, directional solidification conditions are imposed via the boundary conditions on the temperature and concentration fields at infinity:

$$\left[\frac{\partial T^\pm}{\partial z} \right]_{z=\pm\infty} = G^\pm \exp\left(-\frac{V_0}{D_T} z\right), \quad (8)$$

$$C(z \rightarrow +\infty) = C_\infty, \quad (9)$$

where C_∞ is the nominal composition of the alloy and the + and - signs refer to the liquid and solid phases, respectively. The boundary conditions on the thermal field are consistent with exponentially decaying steady-state temperature profiles moving at the uniform isotherm velocity V_0 . The overall conservation of heat condition leads to the relation $G^- = G^+ + (L/c_p)V_0$. It should be emphasized that the two control parameters of the models are G^+ and V_0 , which enter via the boundary condition of the far thermal field. Equations (1)–(9) completely specify the dynamics of the solid-liquid interface for the model.

Additional remarks concerning the quantitative validity of the model and its relevance to rapid solidification experiments should be made:

(i) The velocity-dependent form of k has been found by Aziz *et al.* [21] to hold relatively well for some alloys where experimental values of v_d were determined. However, quantitative values of v_d for alloys where banding has been studied in detail (Al-Fe, Al-Cu, and Ag-Cu) are presently not available. The same is true of the kinetic parameter v^* entering the term representing attachment kinetics. We are therefore forced at present to use estimates of v_d and v^* .

(ii) In slow Bridgman-type directional solidification experiments, the values of the control parameter V_0 and G^\pm are simply related to the pulling speed of the sample and the imposed gradient. In laser or electron-beam surface remelting experiment, the velocity of the solidification front (and hence the V_0) is determined indirectly using the geometrical relation $V_0 = V_b \cos \theta$ [6–8], where V_b is the beam velocity parallel to the surface and θ is the angle between the local orientation of the solidification front and the surface. In contrast to Bridgman-type experiments, V_0 does not remain constant but varies from zero, at the bottom of the remelted zone, to several m/sec at the surface. Modeling such a situation by directional solidification implicitly assumes that V_0 varies sufficiently slowly, on the time scale where the microstructure is formed, to be assumed constant.

(iii) The value of the temperature gradient G at the interface cannot be measured directly and has to be inferred indirectly via a macroscopic heat flow calculation [16]. This leads to an additional uncertainty in this control parameter. Interestingly, the interface dynamics responsible for banding turns out not to be very sensitive to this parameter.

(iv) Using continuum equations of the form (1)–(4) implicitly assumes that the solid-liquid interface can be treated as a sharp interface. This assumption is strictly valid only when the “instantaneous” solutal diffusion length $l_C(t) = D_C/V(t)$ is much larger than the interface thickness $\delta \sim 1$ nm. For the velocity range between 0.1–10 m/s, where the banding cycle typically occurs, l_C can become comparable to or even smaller than δ on the high-velocity end of this range. At this point, the concept of diffusion and the use of the continuum equation breaks down. As a compensating factor, there is the fact that at velocities where this breakdown occurs, the partition coefficient is near unity and solidification becomes essentially diffusionless.

In summary, using the present model of rapid directional solidification, we expect to be able to understand essential features of the interfacial dynamics responsible for banding. However, the accuracy of quantitative predictions is mainly limited by the present uncertainties in nonequilibrium corrections.

III. LINEAR STABILITY

A. Eigenvalue equation

The one-dimensional steady-state diffusion profiles, corresponding to a planar interface moving at constant velocity V_0 , are given by the usual exponentially decaying forms:

$$T_{SS}^\pm(z) = \frac{D_T}{V_0} G^\pm \left[1 - \exp\left(-\frac{V_0}{D_T} z\right) \right] + T_0, \quad (10)$$

$$C_{SS}(z) = C_\infty \left(\frac{1}{k} - 1 \right) \exp\left(-\frac{V_0}{D_C} z\right) + C_\infty, \quad (11)$$

where, as before, the + and – signs refer to the liquid and solid phases, respectively, $G^- = G^+ + (L/c_p)V_0$, and T_0 is the velocity-dependent steady-state temperature of the planar interface determined by the modified Gibbs-Thomson relation (5) with $C_L = C_\infty/k(V_0)$:

$$T_0 \equiv T_{pl}(V_0) = T_M + m(V_0)C_\infty/k(V_0) - \frac{RT_M^2 V_0}{L v^*}. \quad (12)$$

The stability spectrum of the planar interface is then obtained by the standard procedure, which consists in linearizing the equations of motion and interface boundary conditions around the steady-state profiles [(10) and (11)] for sinusoidal perturbations of the form

$$T(x, z, t) = T_{SS}^\pm(z) + \delta T \exp\left(i \frac{2\pi}{\lambda} x \mp \bar{k}^\pm z + \omega t\right), \quad (13)$$

$$C(x, z, t) = C_{SS}(z) + \delta C \exp\left(i \frac{2\pi}{\lambda} x - \bar{k} z + \omega t\right), \quad (14)$$

where \bar{k}^\pm and \bar{k} are related to λ and ω via the diffusion equations (1) and (2). After straightforward algebraic manipulations we obtain the eigenvalue equation for the growth rate $\omega(\lambda)$. We express this equation in terms of the dimensionless growth rate Ω and wave number q defined, respectively, by

$$\Omega = (2D_C/V_0^2)\omega$$

$$q = (2D_C/V_0)2\pi/\lambda.$$

The relation between Ω and q is then given by

$$1 + [1 + \alpha(1 - k) - \beta - \alpha/2]\Omega$$

$$- \frac{1}{2\nu(\Omega)}(1 - 2k) - \gamma(1 - 2k)q^2$$

$$- \left(1 - \frac{1}{2\nu(\Omega)} - \gamma q^2 + \frac{\alpha}{2}\Omega\right) \sqrt{1 + 2\Omega + q^2} = 0, \quad (15)$$

where $\nu(\Omega)$ is defined by

$$\frac{1}{\nu(\Omega)} = \frac{L}{c_p} \frac{k}{mC_0(1 - k)} \text{Le} \left(\frac{\text{Le} + \Omega}{\sqrt{\text{Le}^2 + 2\Omega\text{Le} + q^2}} + 1 \right)$$

$$+ \frac{2D_C}{V_0} \frac{G^+ k}{(1 - k)mC_0}, \quad (16)$$

and α , β , and γ are velocity-dependent functions defined by

$$\beta = \frac{V_0}{(1 - k)} \frac{dk}{dV_0}, \quad (17)$$

$$\alpha = -\frac{\beta}{(1-k_e)} \frac{\ln k/k_e}{m/m_e} - \frac{k}{(1-k)mC_0} \frac{RT_M^2 V_0}{L v^*}, \quad (18)$$

$$\gamma = \frac{\Gamma V_0}{4D_C} \frac{k}{mC_0(1-k)}. \quad (19)$$

Here, Le is the Lewis number

$$Le = \frac{D_C}{D_T}.$$

The coupling between the thermal and concentration fields enters the eigenvalue equation (15) via the function $\nu(\Omega)$ and nonequilibrium effects via the functions α and β .

B. Physical interpretation

There are three essential physical effects that together determine the shape of the stability spectrum $\Omega(q)$ of the planar interface:

(i) The classic MS instability, which, in slow directional solidification, occurs near constitutional supercooling, and, near absolute stability, occurs with decreasing velocity. It results from the competition between the destabilizing effect of the diffusion field and the restabilizing effect of surface tension.

(ii) The CS instability, which originates from the destabilizing effect of solute trapping. Without LHD this instability is most unstable at $q = 0$.

(iii) The effect of LHD, which strongly reduces the amplification rate of a very narrow range of wave number near $q = 0$ and shifts the CS instability to small wave number at absolute stability.

To illustrate how these three effects together shape the stability spectrum, we have found it more illuminating to compare three stability spectra, each spectrum incorporating progressively one more of the above three effects:

(i) The first spectrum, which only contains the first effect, is obtained by setting

$$\alpha = \beta = Le = 0 \quad (\text{MMSS})$$

into Eqs. (15) and (16). It does not include the effect of LHD, since taking the limit $Le = 0$ essentially corresponds to having the thermal field relax instantaneously (i.e., $D_T \rightarrow \infty$). Also, it only contains nonequilibrium effects to the extent that nonequilibrium values of m and k are used. With equilibrium values m_e and k_e , this spectrum is identical to that of the classical MS analysis. We refer hereafter to this spectrum as the modified MS spectrum (MMSS). It is also nearly identical to the one developed by Trivedi and Kurz [24] for rapid solidification, with the minor difference that it does not contain the quasistationary approximation. This difference affects mainly the small-wave-number part of the spectrum that is stable in this approximation.

(ii) The second spectrum, which contains both the first and second effects, is obtained by setting only

$$Le = 0 \quad (\text{FTAS})$$

into Eq. (16). This is the frozen-temperature approxima-

tion spectrum (FTAS) derived previously by Merchant and Davis, which neglects LHD [13].

(iii) The third spectrum is the “full spectrum” (FS) defined by Eq. (15) together with definitions (16)–(19),

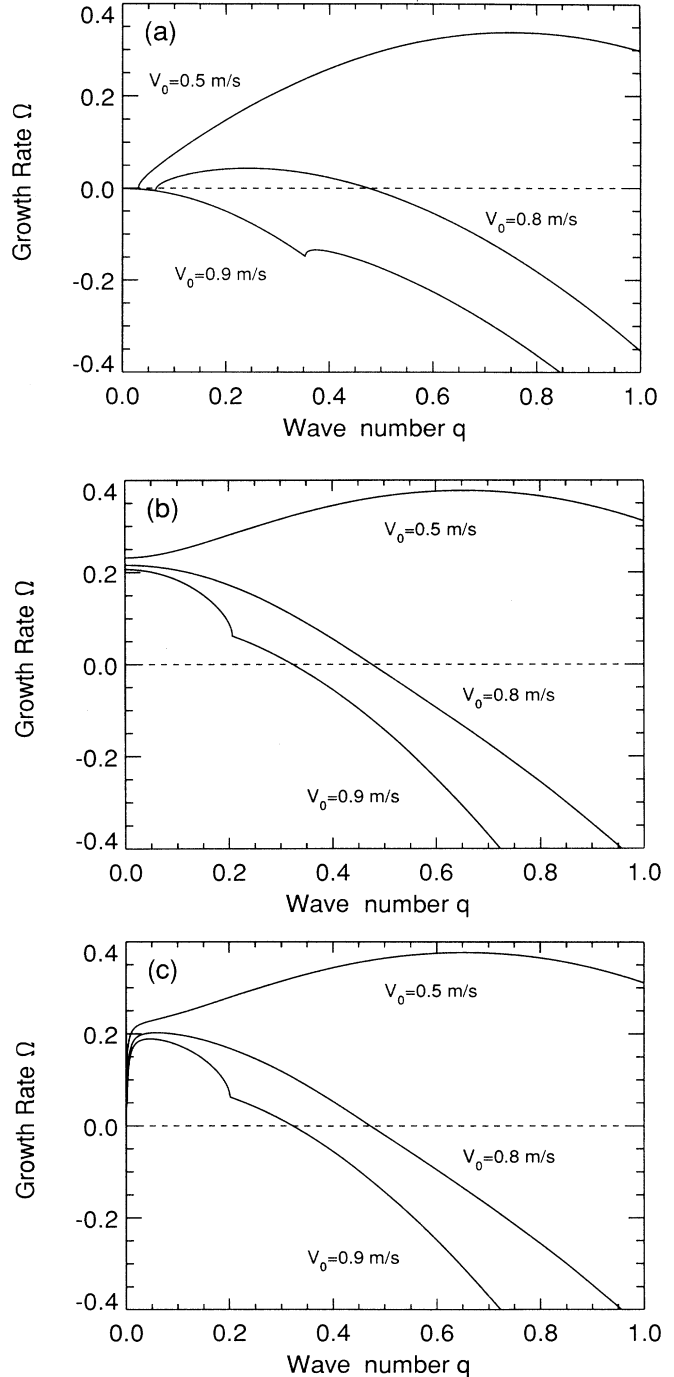


FIG. 2. Real part of $\Omega(q)$ corresponding to the most unstable branch of (a) the modified Mullins-Sekerka spectrum (MMSS) [24], (b) the frozen-temperature-approximation spectrum (FTAS) [13], and (c) the full spectrum (FS), for a 2% wt Fe Al-Fe alloy.

TABLE I. Physical constants used for Al-Fe.

Constant	Value
T_M	933 K
L	10 470 J/mol
c_p	30 J/mol K
k_e	0.037
m_e	-3.5 K/wt %
D_C	$1.7 \times 10^{-9} \text{ m}^2/\text{s}$
D_T	$53.5 \times 10^{-6} \text{ m}^2/\text{s}$ ^a
v^*	2000 m/s ^b
v_d	1.7 m/s ^b
G^+	$5 \times 10^6 \text{ K/m}$ ^b

^aAverage value of solid and liquid diffusivities.

^bValues used in Ref. [16].

which incorporates all three effects.

The real part of $\Omega(q)$ for the MMSS, FTA, and the FS, is plotted respectively in Figs. 2(a)–2(c) for three different velocities. The physical constants used in the present calculations are given in Tables I and II. Only the real part of the most unstable branch is shown, and the imaginary part is not displayed for clarity. The merging of complex conjugate pairs of roots into one real one is responsible for the presence of cusps in the real part of the spectra. A comparison of the FTA and FS at $V_0 = 0.5 \text{ m/s}$ is presented in Fig. 3. The first effect (MS instability) is clearly seen in Fig. 2(a). As the velocity is decreased below the absolute stability limit (equal to $V_0 = 0.87 \text{ m/s}$ for the MMSS), a finite band of wave number q becomes unstable. The small-wave-number part of the spectrum is stable, but with a very small negative real part, which scales as $1/\nu \ll 1$ for $Le = 0$.

The second effect (CS instability) is clearly seen in Fig. 2(b). At $V_0 = 0.9 \text{ m/s}$, where the MMSS is completely stable, the FTA has a band of unstable wave number with the fastest growing mode at $q = 0$. This mode only becomes restabilized at a higher velocity $V_0 \simeq 3 \text{ m/s}$ [not shown in Fig. 2(b)], which constitutes a new absolute stability limit. As the velocity is decreased, the MS instability increases and eventually dominates the

TABLE II. Physical constants used for Al-Cu.

Constant	Value
T_M	933 K
L	10 470 J/mol
c_p	30 J/mol K
k_e	0.14
m_e	-2.6 K/wt %
D_C	$4.9 \times 10^{-9} \text{ m}^2/\text{s}$
D_T	$53.5 \times 10^{-6} \text{ m}^2/\text{s}$ ^a
v^*	1000 m/s ^b
v_d	4.9 m/s ^b
G^+	$5 \times 10^6 \text{ K/m}$ ^b

^aAverage value of solid and liquid diffusivities.

^bValues used in Ref. [16].

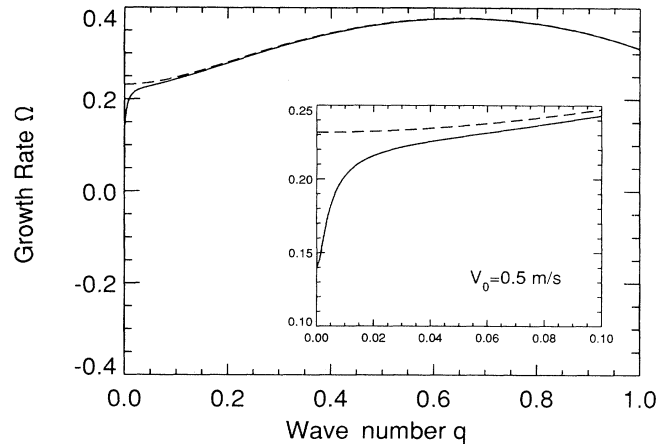


FIG. 3. Comparison of the FTAS [13] and FS.

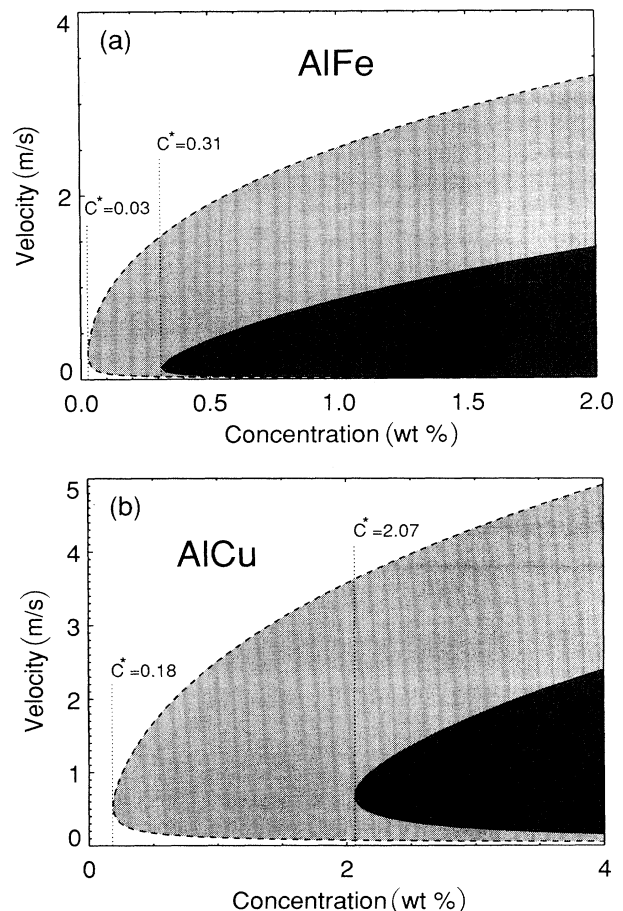


FIG. 4. Neutral stability boundaries of the $q = 0$ planar instability: (a) Al-Fe, and (b) Al-Cu. The light and dark shaded regions correspond to unstable regions, as predicted respectively by the FTAS [13] (light) and FS (dark). The upper neutral stability boundary of the planar instability for the FTAS also corresponds to the absolute stability limit of the FS. C^* indicates the lower critical composition below which banding should not occur. Note that C^* is underestimated by the FTAS.

$q = 0$ instability. This crossover is shown in Fig. 2(b), where at $V_0 = 0.5$ m/s, the MS instability dominates the $q = 0$ instability (i.e., it has a larger amplification rate), while at $V_0 = 0.9$ m/s it is the $q = 0$ instability that dominates.

The last effect (LHD) is shown in Figs. 2(c) and 3. The very-small-wave-number part of the FTA is strongly restabilized by the effect of LHD. Consequently, the CS instability becomes shifted to a small finite wave number. This is clearly seen in the FS at $V_0 = 0.9$ m/s in Fig. 2(c), where the most unstable mode is at a q slightly less than 0.1, in contrast to $q = 0$ in Fig. 2(b). As before, the CS instability becomes restabilized at a new absolute stability limit $V_0 \simeq 3$ m/s, and, with decreasing velocity, the wave number of the most unstable modes increases abruptly as a consequence of the crossover from the CS instability to the MS instability. Figure 3 has been included to illustrate the fact that latent-heat diffusion only affects the very-small-wave-number part of the FTA. This feature is a direct consequence of the smallness of the Lewis number and is explored further at the end of Sec. V.

The most relevant consequence of the effect of LHD on banding, as seen from linear stability analysis, is the reduction of the parameter range where banding should occur. We see in Figs. 4(a) and 4(b) that the domains of the composition-velocity plane where the planar instability, assumed to trigger banding, occurs is dramatically reduced by LHD. In particular, the FTA grossly underestimates the critical alloy composition C^* below which

banding should be absent. In Al-Cu Zimmermann, Carrard, and Kurz [7] still observe bands at 3 wt % Cu but not at 1 wt % Cu. The value $C^* \simeq 2$ wt % determined with LHD is therefore in good agreement with these observations. In Al-Fe, bands have been observed to persist down to compositions as small as 0.25 wt % Fe [8] while we predict here bands not to form below $C^* \simeq 0.3$ wt % Fe. Note that this value is only slightly larger than 0.25 wt % Fe.

Finally, we note that the absolute stability limit V_{AS} with and without LHD is the same (see the end of Sec. V). The only difference is the value of the critical wave number, which is shifted to a finite value with latent-heat diffusion. Consequently, the upper stability boundary of the $q = 0$ mode for the FTAS in Figs. 4(a) and 4(b) also corresponds to the absolute stability limit of the FS.

IV. BOUNDARY INTEGRAL FORMULATION

To investigate the nonlinear dynamics of our model, we recast the equations of interface motion in the form of coupled integral equations for the composition and thermal fields using the standard Green's-function approach [25, 26].

A. Two dimensions

For a general nonplanar interface in two dimensions these equations take the form

$$\frac{C_L}{2} = \int_0^t dt' \int_{S(t')} dx' C_L G_{2D}(\Delta\xi, \Delta x; \Delta t) \left[\frac{\Delta\xi}{2\Delta t} - \frac{\partial\xi'}{\partial x'} \frac{\Delta x}{2\Delta t} - k \frac{\partial\xi'}{\partial t'} \right] + \int_{S(0)} dx' dz' G_{2D}(\xi - z', \Delta x; t) C(x', z', 0), \quad (20)$$

$$T_i = \frac{L}{c_p} \text{Le} \int_0^t dt' \int_{S(t')} dx' G_{2D}(\sqrt{\text{Le}}\Delta\xi, \sqrt{\text{Le}}\Delta x; \Delta t) \frac{\partial\xi'}{\partial t'} + \text{Le} \int_{S(0)} dx' dz' G_{2D}(\sqrt{\text{Le}}[\xi - z'], \sqrt{\text{Le}}\Delta x; t) T(x', z', 0), \quad (21)$$

where the 2D diffusion Greens function is given by

$$G_{2D}(u, v; \tau) = \frac{1}{4\pi D_C \tau} \exp\left(-\frac{u^2 + v^2}{4D_C \tau}\right). \quad (22)$$

Here, $C(x, z, 0)$ and $T(x, z, 0)$ are, respectively, the initial concentration and temperature profiles, $S(t)$ denotes the interface profile at time t , and $\xi(x, t)$ measures the vertical interface displacement in the z direction in a stationary frame. We have also defined $\xi' \equiv \xi(x', t')$,

$\Delta\xi \equiv \xi - \xi'$, $\Delta x \equiv x - x'$, and $\Delta t \equiv t - t'$. These equations completely determine the motion of the interface together with the modified Gibbs-Thomson condition (5) which relates C_L and T_i .

B. One dimension

For a planar interface in one dimension, the boundary integral equations are reduced after integration over x' to the form

$$\frac{C_L(t)}{2} = \int_0^\infty dz' C(z', 0) G_{1D}(\xi(t) - z'; t) + \int_0^t dt' C_L(t') \left(\frac{1}{2} \frac{\xi(t) - \xi(t')}{t - t'} - k(t') \frac{d\xi(t')}{dt'} \right) G_{1D}(\xi(t) - \xi(t'); t - t'), \quad (23)$$

$$T_i(t) = \sqrt{\text{Le}} \int_{-\infty}^\infty dz' T(z', 0) G_{1D}(\sqrt{\text{Le}}[\xi(t) - z']; t) + \frac{L}{c_p} \sqrt{\text{Le}} \int_0^t dt' \frac{d\xi(t')}{dt'} G_{1D}(\sqrt{\text{Le}}[\xi(t) - \xi(t')]; t - t'), \quad (24)$$

where the interface position $\xi(t)$ is now independent of x and the 1D diffusion Green's function is given by

$$G_{1D}(u; \tau) = \frac{1}{\sqrt{4\pi D_C \tau}} \exp\left(-\frac{u^2}{4D_C \tau}\right). \quad (25)$$

Both for the numerics and for the small Lewis number analysis, it is useful to rewrite the first integral on the RHS of Eq. (24) by choosing the initial temperature profile $T(z', 0)$ equal to the steady-state profile $T_{SS}^\pm(z')$ [Eq. (10)]. This choice of initial condition is not limiting since we are interested here in following the evolution of a perturbed planar interface into nonlinear regimes. The nonlinear cycles of oscillations of the planar inter-

face are independent of the initial profiles at sufficiently large times.

Substituting $T(z', 0) = T_{SS}^\pm(z')$ into Eq. (24) (where the $-$ and $+$ signs refer respectively to the interval $[-\infty, 0]$ and $[0, \infty]$) and using the identity

$$\int_{-\infty}^{\infty} \frac{dz'}{\sqrt{4\pi D_T t}} \exp\left(-\frac{[\xi(t) - z']^2}{4D_T t} - \frac{V_0}{D_T} z'\right) = \exp\left(-\frac{V_0}{D_T} [\xi(t) - V_0 t]\right), \quad (26)$$

we find after simple manipulation that the integral equation for the temperature field can be rewritten in the form:

$$T_i(t) - T_0 = G^+ \frac{D_T}{V_0} \left[1 - \exp\left(-\frac{V_0}{D_T} [\xi(t) - V_0 t]\right)\right] + \frac{L}{c_p} \sqrt{\text{Le}} \int_{-\infty}^0 dz' G_{1D}(\sqrt{\text{Le}}[\xi(t) - z']; t) \left[1 - \exp\left(-\frac{V_0}{D_T} z'\right)\right] + \frac{L}{c_p} \sqrt{\text{Le}} \int_0^t dt' \frac{d\xi(t')}{dt'} G_{1D}(\sqrt{\text{Le}}[\xi(t) - \xi(t')]; t - t'). \quad (27)$$

V. SMALL LEWIS NUMBER LIMIT: DERIVATION OF A REDUCED TEMPERATURE EQUATION

There are three essential reasons that render the analysis of the small Lewis number limit particularly relevant here:

(i) In metallic alloys, the Lewis number is typically on the order of 10^{-4} and can therefore be treated as a small parameter.

(ii) In this limit the integral equation for the temperature field can be rewritten in the form of a reduced temperature equation (RTE) corresponding to the first two leading terms in an asymptotic expansion in Le of the boundary integral for the thermal field. This form is numerically simpler to handle but remains quantitatively accurate. In the 2D case, describing nonplanar dynamics, the RTE takes the form of a one-dimensional integral equation only involving a spatial average over the interface velocity $\partial\xi/\partial t$. This renders the 2D problem considerably more tractable numerically.

(iii) The RTE provides a basis for an analytical understanding of the role of latent heat diffusion, which plays a crucial role in banding (Sec. VIC 1).

We first give a formal derivation of the RTE for the one-dimensional case of primary interest here. We then provide an alternate derivation based on scaling arguments, which provides a better physical understanding of this equation; and write down an equivalent Fourier series representation, which leads to more efficient numerics. Finally, we provide a derivation for the 2D case.

A. One dimension

The reason for rewriting Eq. (24) in the form of Eq. (27) becomes apparent when considering the small Le

limit. At leading order in Le , the second and third terms on the RHS of Eq. (27) drop out. The equation for the temperature field becomes simply

$$T_i(t) - T_0 = G^+ \frac{D_T}{V_0} \left(1 - \exp\left[-\frac{V_0}{D_T} [\xi(t) - V_0 t]\right]\right). \quad (28)$$

At this order, we recover the frozen-temperature approximation (FTA) mentioned earlier, which neglects entirely the effect of LHD. For $\xi(t) - V_0 t \ll D_T/V_0$, Eq. (28) reduces to the more familiar form of the FTA

$$T_i(t) - T_0 = G^+ [\xi(t) - V_0 t], \quad (29)$$

which assumes motion in a straight temperature profile.

Next, we evaluate the first contribution beyond leading order in Le (i.e., beyond the FTA) originating from the second and third terms on the RHS of Eq. (27). To make the small parameter Le appear explicitly it is useful to scale spatial coordinates by the solutal diffusion length $l_C = D_C/V_0$ and time in units of the solutal diffusion time $\Gamma_C = D_C/V_0^2$ using the substitutions

$$\begin{aligned} \xi &\rightarrow \xi/l_C, \\ z &\rightarrow z/l_C, \\ t &\rightarrow t/\Gamma_C. \end{aligned} \quad (30)$$

After performing these scale transformations, Eq. (27) becomes

$$T_i(t) - T_0 = \tilde{G}^+ \frac{1}{\text{Le}} (1 - \exp\{-\text{Le}[\xi(t) - t]\}) + \frac{L}{c_p} \sqrt{\text{Le}} \int_{-\infty}^0 \frac{dz'}{\sqrt{4\pi t}} \exp\left(-\text{Le} \frac{[\xi(t) - z']^2}{4t}\right) [1 - \exp(-\text{Le}z')] \\ + \frac{L}{c_p} \sqrt{\text{Le}} \int_0^t \frac{dt'}{\sqrt{4\pi(t-t')}} \frac{d\xi(t')}{dt'} \exp\left(-\text{Le} \frac{[\xi(t) - \xi(t')]^2}{4(t-t')}\right), \quad (31)$$

where we have defined the scaled temperature gradient $\tilde{G}^+ = G^+ D_C / V_0$. The dominant contribution of the last term on the RHS of Eq. (31) becomes

$$\frac{L}{c_p} \sqrt{\text{Le}} \int_0^t \frac{dt'}{\sqrt{4\pi(t-t')}} \frac{d\xi(t')}{dt'} + \dots, \quad (32)$$

which comes from replacing the exponential factor by unity. Here the ellipsis denotes higher-order corrections in Le . In the second term on the RHS of Eq. (31), the space integral over z' runs over the interval $[-\infty, 0]$, and the exponential factors cannot simply be replaced by unity. To extract the dominant contribution of this integral, we make the change of variable

$$u = \sqrt{\frac{\text{Le}}{4t}} [\xi(t) - z'], \quad (33)$$

after which it can be rewritten in the form

$$\frac{L}{c_p} \int_{\xi(t)\sqrt{\text{Le}/4t}}^{+\infty} \frac{du}{\sqrt{\pi}} \exp(-u^2) \\ \times \{1 - \exp[-\text{Le}\xi(t) + u\sqrt{4t\text{Le}}]\}. \quad (34)$$

In this form, the exponential containing terms proportional to Le and $\sqrt{\text{Le}}$ can now be expanded and the lower limit of the integral replaced by zero. The integral then becomes

$$-\frac{L}{c_p} \sqrt{\text{Le}} \int_0^{+\infty} \frac{du}{\sqrt{\pi}} \exp(-u^2) u \sqrt{4t} + \dots \\ = -\frac{L}{c_p} \sqrt{\text{Le}} \sqrt{\frac{t}{\pi}} + \dots \quad (35)$$

Finally, using the identity

$$\sqrt{\frac{t}{\pi}} = \int_0^t \frac{dt'}{\sqrt{4\pi(t-t')}} \quad (36)$$

and combining Eqs. (31)–(36), we obtain the RTE:

$$T_i(t) - T_0 = \tilde{G}^+ [\xi(t) - t] \\ + \frac{L}{c_p} \sqrt{\text{Le}} \int_0^t \frac{dt'}{\sqrt{4\pi(t-t')}} \left(\frac{d\xi(t')}{dt'} - 1 \right). \quad (37)$$

It is also useful to express the RTE in terms of the original dimensional space and time coordinates where it becomes

$$T_i(t) - T_0 = G^+ [\xi(t) - V_0 t] \\ + \frac{L}{c_p} \int_0^t \frac{dt'}{\sqrt{4\pi D_T(t-t')}} \left(\frac{d\xi(t')}{dt'} - V_0 \right). \quad (38)$$

The steady-state solution

$$\xi(t) = V_0 t \quad (39)$$

is trivially seen to be a solution of the RTE. Note that Eq. (38) has the form of Abel's equation first derived for the problem of finding the form of a plane curve along which a particle can fall in a time that is a prescribed function of vertical distance.

B. Alternate derivation

We include here an alternate derivation of the RTE based on scaling arguments, which provides more physical insight into its origin and thermal effects in general. This derivation starts by noting that the scale ζ_T on which the temperature profile is perturbed during the oscillation cycle

$$\zeta_T \sim \sqrt{D_T \Gamma_{\text{osc}}}, \quad (40)$$

where Γ_{osc} is the period of oscillation, is much larger than the scale ζ characterizing the displacement of the interface in the frame of the moving isotherm. A good measure of the latter is the root-mean-square displacement of the interface averaged over some time $T \gg \Gamma_{\text{osc}}$

$$\zeta = \sqrt{\frac{1}{T} \int_0^T dt [\xi(t) - V_0 t]^2} \quad (41)$$

[the average of $\xi(t) - V_0 t$ is identically zero following the requirement that, on the average, the interface moves with the isotherm velocity V_0].

One part of the interfacial temperature variations comes from the motion of the interface in the underlying temperature profile and is given by the first term on the RHS of Eq. (37). It follows from the condition $\zeta_T \gg \zeta$ that the additional part originating from the excess (positive or negative) heat flux generated by the unsteady motion of the interface can be calculated as though the interface remained stationary in the frame of the moving isotherm. Since the additional heat flux generated by this unsteady motion is proportional to

$$\frac{L}{c_p} \left(\frac{d\xi(t)}{dt} - V_0 \right), \quad (42)$$

it follows that the additional temperature variations are given by the solution of the heat diffusion equation with a steady moving point source

$$D_T \frac{\partial^2 T}{\partial y^2} + V_0 \frac{\partial T}{\partial y} - \frac{\partial T}{\partial t} = -\frac{L}{c_p} \left(\frac{d\xi(t)}{dt} - V_0 \right) \delta(y), \quad (43)$$

where $y \equiv z - V_0 t$ is the space coordinate in the frame of the moving isotherm. The final step consists in recogniz-

ing that the advection term $V_0 \partial T / \partial y$ can be neglected in Eq. (43). This follows from the fact that the period of oscillation of the interface Γ_{osc} is much smaller than the thermal diffusion time $\Gamma_T \equiv D_T / V_0^2$ or, equivalently, that $\zeta_T \ll l_T$. Consequently,

$$\frac{\partial^2 T}{\partial y^2} \sim \frac{1}{\zeta_T^2} \gg \frac{V_0}{D_T} \frac{\partial T}{\partial y} \sim \frac{1}{\zeta_T l_T}. \quad (44)$$

Neglecting the advection term, the part of the interfacial temperature variations due to the excess heat flux generated by unsteady motion is then given by the solution at $y = 0$: $T(y = 0, t)$ of the heat equation with an effectively stationary heat source

$$D_T \frac{\partial^2 T}{\partial y^2} - \frac{\partial T}{\partial t} = -\frac{L}{c_P} \left(\frac{d\xi(t)}{dt} - V_0 \right) \delta(y). \quad (45)$$

It is then elementary to show that $T(y = 0, t)$ is given identically by the second term on the RHS of Eq. (37) leading to the same previously derived RTE.

C. Fourier series representation

Although the integral representation of the RTE [Eq. (38)] is more suitable for analytical treatment, its equivalent Fourier series representation (FSR) leads to considerably more efficient numerics. The FSR can be derived by seeking directly a solution of $T(y = 0, t)$ of Eq. (45) in the form of a Fourier series. Since the solution is even [i.e., $T(-y, t) = T(y, t)$], $T(y, t)$, it can be expanded in a Fourier cosine series of the form

$$T(y, t) = \frac{a_0(t)}{2} + \sum_{j=1}^M a_j(t) \cos \frac{j\pi y}{L_0} \quad (46)$$

over the interval $y = [-L_0, L_0]$. The only constraint on the box-size L_0 is that it should be sufficiently larger than the scale ζ_T characterizing the variations of the thermal field, such that the solution does not depend on L_0 . Accordingly, for a given L_0 , the number of modes M should be chosen large enough for the solution to converge to some desired accuracy.

Substituting the series (46) into the heat equation (45), and adding the contribution to interfacial temperature variations coming from the motion of the interface in the underlying temperature profile [i.e., the FTA contribution equal to the first term on the RHS of Eq. (38)], we obtain the FSR of the RTE in the form

$$\begin{aligned} \frac{da_j(t)}{dt} = & -D_T \left(\frac{j\pi}{L_0} \right)^2 a_j(t) \\ & + \frac{L}{c_P} \frac{1}{L_0} \left(\frac{d\xi(t)}{dt} - V_0 \right), \quad j = 0, M \end{aligned} \quad (47)$$

$$T_i(t) - T_0 = \frac{a_0(t)}{2} + \sum_{j=1}^M a_j(t) + G^+[\xi(t) - V_0 t]. \quad (48)$$

The numerical advantage of the FSR over the integral representation [Eq. (38)] comes from the fact that the equations for the a_j are local in time. Thus, for a computation of N time steps the cost of evaluating $T_i(t)$ by the integral representation scales as N^2 , while the cost of evaluating the FSR scales as NM , which is considerably more efficient at large time ($N \gg M$).

D. Two dimensions

We provide here a derivation of the RTE in 2D appropriate for studying nonplanar dynamics. The derivation follows essentially the same line as in one dimension and we only point out the main differences. As before, we consider the initial value problem corresponding to a steady-state planar temperature profile $T(x, z, 0) = T_{\text{SS}}^\pm(z)$. After substitution of this initial profile in the integral, Eq. (21), the second term on the RHS can be rewritten in the limit $\text{Le} \ll 1$ as the sum of two terms equal to the FTA contribution given by Eq. (29) and a spatial integral that reduces as before to Eq. (35).

The main difference from the 1D case comes from the time integral corresponding to the first term on the RHS of Eq. (21). To analyze this term, we again perform the scale transformation (30) after which it can be written in the form

$$\frac{L}{c_P} \text{Le} \int_0^t dt' \int_{S(t')} dx' G_{2D}(\sqrt{\text{Le}} \Delta \xi, \sqrt{\text{Le}} \Delta x; \Delta t) \frac{\partial \xi'}{\partial t'} = \text{Le} \frac{L}{c_P} \int_0^t \frac{dt'}{4\pi(t-t')} \int_{-\infty}^{+\infty} dx' \exp\left(-\text{Le} \frac{(x-x')^2}{4(t-t')}\right) \frac{\partial \xi}{\partial t'}, \quad (49)$$

where we have used the fact that

$$\exp\left(-\text{Le} \frac{[\xi(t) - \xi(t')]^2}{4(t-t')}\right) = 1 + \dots \quad (50)$$

Note that the exponential factor in (49) cannot be approximated by unity because the integral over x' runs over the interval $[-\infty, \infty]$. Next, we express the interface displacement $\xi(x', t')$ in terms of a Fourier series of the form

$$\xi(x', t') = \sum_n c_n(t') e^{-in2\pi x' / \tilde{L}_x}, \quad (51)$$

where \tilde{L}_x is the scaled system width ($\tilde{L}_x = L_x / l_C$). Substituting the above form into Eq. (49), completing the square of the exponential, and evaluating the remaining Gaussian integral, we obtain

$$\begin{aligned} \frac{L}{c_p} \text{Le} \int_0^t dt' \int_{S(t')} dx' G_{2D}(\sqrt{\text{Le}}\Delta\xi, \sqrt{\text{Le}}\Delta x; \Delta t) \frac{\partial \xi'}{\partial t'} \\ = \sqrt{\text{Le}} \frac{L}{c_p} \sum_n e^{-in2\pi x/\bar{L}_x} \int_0^t \frac{dt'}{\sqrt{4\pi(t-t')}} \exp\left(-\left[\frac{2\pi n}{\sqrt{\text{Le}}\bar{L}_x}\right]^2 (t-t')\right) \frac{dc_n(t')}{dt'}; \quad (52) \end{aligned}$$

It is now apparent that in the small Le number limit the only term which survives in the above sum corresponds to $n = 0$. This term together with the FTA contribution [Eq. (28)] and the spatial integral contribution [Eq. (35)] yields the 2D RTE, which, after converting back to unscaled coordinates, takes the form

$$\begin{aligned} T_i(t) - T_0 = G^+[\xi(t) - V_0 t] \\ + \frac{L}{c_p} \int_0^t \frac{dt'}{\sqrt{4\pi D_T(t-t')}} \left(\frac{d\langle \xi \rangle}{dt'} - V_0 \right), \quad (53) \end{aligned}$$

where

$$\frac{d\langle \xi \rangle}{dt'} = \frac{1}{L_x} \int_0^{L_x} dx' \frac{\partial \xi'(x', t')}{\partial t'}. \quad (54)$$

We note that the only difference between the 1D and 2D RTE is that the velocity of the interface $d\xi(t')/dt'$ in Eq. (38) is substituted by the spatial average of the vertical velocity of the interface $d\langle \xi \rangle/dt'$ in 2D. In terms of the alternate derivation of the RTE given above, this reflects the fact that in 2D the total heat flux generated by the unsteady motion of the interface is simply given by

$$\frac{L}{c_p} \left(\frac{d\langle \xi \rangle}{dt} - V_0 \right). \quad (55)$$

For numerical purposes the method of choice is to use a FSR of the RTE which in 2D is given by Eqs. (47) and (48) with the substitution $d\xi(t)/dt \rightarrow d\langle \xi \rangle/dt$.

Linear stability spectrum revisited

A question that arises in the present context is to what extent the 2D RTE [Eq. (53)] together with the exact integral equation for the concentration field reproduce the full stability spectrum. This question is answered at once by noting that for sinusoidal linear perturbations of the form (13) and (14) the spatial average $d\langle \xi \rangle/dt$ is always zero except at zero wave number. The spectrum obtained with the RTE (RTES) is then given exactly, for $q \neq 0$, by the frozen-temperature approximation spectrum (FTAS) defined in Sec. II and, for $q = 0$, by the eigenvalue equation (15) with

$$\begin{aligned} \frac{1}{\nu(\Omega)} = \frac{L}{c_p} \frac{k}{mC_0(1-k)} \sqrt{\frac{\text{Le}\Omega}{2}} \\ + \frac{2D_C}{V_0} \frac{G^+k}{(1-k)mC_0}, \quad (56) \end{aligned}$$

which represents a very good approximation of the previous definition of $1/\nu(\Omega)$ [Eq. (16)] for small Le. The spectrum is therefore discontinuous at $q = 0$.

The origin of this discontinuity is linked to our previous observation in Sec. II (see Fig. 3) that latent-heat diffusion only affects the very-small-wave-number part of the FTAS. In particular, the width of the thin boundary layer of small wave numbers restabilized by LHD shrinks to zero in the $\text{Le} \rightarrow 0$ limit. Thus, the only feature of the FS lost with the RTE is the existence of a finite width to this thin boundary layer. To study the long-wavelength modulations of the interface near absolute stability described by Coriell and Sekerka [11] (or long-wavelength modulations of the banded structure itself), which are linked to the existence of a maximum growth rate at small q , the RTE is not adequate. However, the RTE provides an excellent approximation to investigate the alternation between a $q = 0$ planar structure and a cellular structure with a wave number $q \neq 0$ well outside this boundary layer. It is this alternation of structure that is believed to be responsible for banding.

Finally, we note that the fact that the absolute stability limits of the FTAS and the FS are identical can easily be derived from the above spectrum. In particular, the absolute stability limit of the FS in the small Lewis number limit is given by that of the RTES. The most unstable mode of the latter at V_{AS} is given by the limit $q \rightarrow 0^+$ of $\Omega(q)$, which is therefore identical to that of the FTAS.

VI. INTERFACE DYNAMICS

In this section we investigate the unsteady dynamics of the “planar” interface and the role of thermal effects in connection with banding. As explained at length in Sec. III and at the end of the preceding section the $q = 0$ mode is no longer the most unstable one in the presence of LHD, even in a velocity range where the larger q MS-type instability is suppressed [see, for example, Fig. 2(c)]. Nevertheless, we choose to study the nonlinear dynamical evolution of this “not-most-unstable mode.” There are several justifications for this choice:

(i) Experimental observations generically show that bands occur parallel to the solidification front, indicating an essentially planar dynamics of the interface, at least during the formation of the light microsegregation-free bands.

(ii) The small q instabilities, which are more unstable than the $q = 0$ one at the level of linear stability, may lead to very-long-wavelength transverse modulations of the banded structure, which are sometimes seen. By selecting the $q = 0$ mode we are essentially neglecting these modulations. It should also be noted that the rapid acceleration of the interface following the $q = 0$ instability compresses the boundary layer of solute ahead of the interface (with a thickness $\sim D_C/V$), thereby suppressing

all finite q instabilities during part of the oscillatory cycles.

(iii) During its oscillation cycle, the planar interface traverses a low-velocity regime where larger q (MS-type) unstable modes, which differ from the aforementioned small q unstable modes, should lead to a spatially periodic cellularlike structure that is automatically suppressed by restricting the dynamics to being planar. We therefore cannot describe this transverse structure or study to what degree its occurrence would affect the shape and duration of the overall oscillation cycle that determines the band spacing. Although this represents a serious limitation to characterize banded structures where both light and dark bands have comparable widths, we expect to be able to characterize by planar oscillations the total width of those structures, occurring at higher isotherm velocities, where the light bands are considerably wider than dark ones. In particular, when $\lambda_{\text{dark}}/\lambda_{\text{light}} \ll 1$, the interface should remain nearly planar during a major portion of its oscillation cycle, spending only a short time in a nonplanar morphology, which is expected not to affect much the overall cycle of oscillation.

(iv) The amplitude of oscillations of the planar interface grows initially as $\sqrt{V_c - V_0}$. Thus, we expect the small-amplitude oscillations occurring in the neighborhood of V_c not to be particularly relevant to banding. Those would undoubtedly be strongly modulated by small q instabilities. However, as V_0 is decreased away from its threshold value V_c , the character of oscillations changes rapidly from small-amplitude sinusoidal oscillations to large-amplitude relaxation oscillations. It is the latter that we expect to be responsible for banding. Also, as argued in (ii) above, these are expected to be less affected by long-wavelength modulations.

A. Numerics

1. Two distinct formulations

To study the dynamics of the planar interface, we have solved two distinct formulations of the free-boundary problem given by Eqs. (1)–(5), together with the non-equilibrium corrections and boundary conditions given by Eqs. (6)–(9):

(1) *Exact formulation.* Consisting of the boundary integrals for the diffusion fields with initial steady-state profiles: Eq. (23) for $C_L(t)$ with $C(z', 0) = C_{\text{SS}}(z')$, Eq. (27) for $T_i(t)$, and Eq. (5), which couples $T_i(t)$ and $C_L(t)$ on the interface.

(2) *Reduced formulation.* Consisting of the boundary integral formulation for the concentration field with an initial steady-state profile coupled to the RTE (which inherently assumes an initial steady-state profile): Eq. (23) with $C(z', 0) = C_{\text{SS}}(z')$, Eqs. (47) and (48) for $T_i(t)$, and Eq. (5).

The only difference between the two formulations is the representation of the thermal field, which is exact in (1) and approximate in (2). Due to the smallness of the Lewis number, $\text{Le} \simeq 3 \times 10^{-5}$ in the Al-Fe alloy, and

metallic alloys in general, the reduced formulation (2) yields results that are very close to those obtained using the exact formulation (1). In the present investigation, we mainly use the exact formulation (1) to study interface dynamics. We have used the reduced formulation mainly to check, as a testing ground for 2D, that it does indeed represent a good approximation of (1) in 1D, and to study the spatiotemporal variations of the thermal profile.

2. Methodology

To solve numerically the exact formulation (1) we have used a straightforward method that consists in evaluating the integrals using appropriate quadrature formulas and a two-dimensional Newton method to solve for the two unknowns $C_L(t)$ and $\xi(t)$ at each time step. The third unknown $T_i(t)$ is eliminated via the Gibbs-Thomson condition (5). Two types of integrals appear in Eqs. (23) [with $C(z', 0) = C_{\text{SS}}(z')$] and (27): spatial integrals over z' and time integrals over t' . The spatial integrals are calculated efficiently by rewriting them in the form of complementary error functions. The numerical cost of evaluating these integrals remains constant as t increases and represents a negligible part of the computation.

The integrals over t' are evaluated by using a quadrature formula designed to handle the square-root singularity of the integrand $\sim 1/\sqrt{t-t'}$. The time interval $[0, t]$ is divided into N intervals

$$0, t_1, t_2, \dots, t_i, \dots, t_{N-1}, t_N,$$

which are not necessarily equally spaced. The freedom of handling nonequally spaced time intervals turns out to be particularly crucial in this study due to the fact that the interface velocity changes abruptly by about one order of magnitude during the oscillation cycles. The time integrals have the generic form

$$I = \int_0^{t_N} dt' \frac{f(t', t_N)}{\sqrt{t_N - t'}} = \sum_{i=0}^{N-1} \int_{t_i}^{t_{i+1}} dt' \frac{f(t', t_N)}{\sqrt{t_N - t'}},$$

where the square-root dependence has been singled out and $f(t', t_N)$ represents all the other terms inside the integrand. The function $f(t', t_N)$ is then approximated by a linear interpolation formula of the form

$$f(t', t_N) = f_{N,i} \frac{t_{i+1} - t'}{t_{i+1} - t_i} + f_{N,i+1} \frac{t' - t_i}{t_{i+1} - t_i}$$

over each interval $t' = [t_i, t_{i+1}]$ where $f_{N,i} \equiv f(t_N, t_i)$. Substituting this form into the above expression for I , we obtain a quadrature formula of the form

$$I = \sum_{i=0}^N w_{N,i} f_{N,i},$$

where the weights $w_{N,i}$ are obtained by evaluating analytically the integral over t' within each interval, the square root singularity of the integrand being removed.

For the reduced formulation (2), we use the same methodology to evaluate the integral equation for the

concentration field and a second-order implicit scheme to time step the a_j in Eq. (47).

3. Efficiency and accuracy considerations

The accuracy of our numerical calculations is mainly limited by the accuracy of the quadrature formula used to evaluate the time integrals of the form I , which scale as $N\Delta t^3$ where $N = t/\Delta t$ is the total number of time step. For the reduced formulation (2), the time stepping of the a_j leads to an error of order Δt^3 at each time step and to a total error of the same order.

With regard to the efficiency of the methods, the costly part of the computation at large N comes from the time integral for the temperature field. Due to the smallness of Le , the concentration field has a much shorter memory than the temperature field. In particular, it decays on a time scale much shorter than Γ_{osc} . Consequently, the computational cost necessary to evaluate the time integral for $C_L(t)$ scales as RN , where R is a cutoff beyond which the integrand is vanishingly small. (It varies here between 100 and 500.) On the contrary, the temperature field has a long-term memory with a characteristic decay rate $\sim D_T/V_{min}^2$ longer than the period of oscillation. The computational cost necessary to evaluate the time integral for $T_i(t)$ therefore scales as $N^2 \gg RN$.

For the reduced formulation (2), the cost of evaluating the concentration integral remains the same, but the cost of evaluating the temperature field is greatly reduced. The computational cost to time step the a_j scales as MN for large N where M (the number of Fourier modes) remains constant in time. Here, we used values of M ranging between 500 and 3000.

We conclude by noting that, in 1D, both formulations (1) and (2) lead to reasonable computing times, (2) being more efficient than (1). However, in 2D, the analog of the exact formulation (1) is numerically too costly to carry out, even on fastest current machines, mainly because of the inherent stiffness of the equations related to the smallness of the Lewis number. Using an accelerated algorithm for the thermal field, such as the ones recently developed by Strain [27] or Brattkus and Meiron [15], would considerably reduce the computations. However, it would not cure the present problem of having two diffusion fields with vastly different time scales and spatial scales. The Fourier representation of the 2D RTE eliminates the spatial stiffness of the equations by reducing the equation for the 2D temperature field to an effectively 1D problem whose computation cost scales as NM as in 1D. The problem of the thermal field being removed, the computation of the concentration field should then be manageable using the integral representation [Eq. (23)] or, more efficiently, accelerated algorithms.

B. Frozen-temperature limit and the CGZK model

In this part, we first review briefly the CGZK model and then compare the cycle it predicts with the cycle of oscillation of the planar interface calculated numerically using the FTA [Eq. (28)]. Oscillation cycles using the

FTA have also been reported in Refs. [14] and [15]. The goal here is to first investigate the validity of this model within the approximation on which it is based. We shall see later that the inclusion of LHD dramatically alters the character of the FTA cycles.

1. The CGZK model

The CGZK model of banding starts with the observation that at high velocity there exists a range of interfacial temperature over which steady-state solidification can proceed at three distinct velocities. As an illustration, we show in Fig. 5 the case of 2 wt % Fe Al-Fe alloys. All the calculations of the present paper have been performed at this composition. The lowest velocity corresponds to a steady-state dendrite branch which merges near point 1 with the steady-state branch of the planar interface. We denote by $T_{den}(V)$ the dendrite branch and by $T_{pl}(V)$ the planar branch. The latter has, with increasing velocity, an up-sloping part from point 1 to point 3 ($V_1 < V < V_3$) and a down-sloping part after point 3 ($V > V_3$).

For a fixed isotherm velocity V_0 , the steady-state temperature of the interface is given by $T_{den}(V_0)$ for $V_0 < V_1$ and $T_{pl}(V_0)$ for $V_0 > V_3$. However, for $V_1 < V_0 < V_3$, it is assumed in the CGZK model that the up-sloping branch of the $T_{pl}(V)$ is unstable, in contrast to the down-sloping part, which is stable. As a consequence, steady-state solidification is no longer possible, and, instead, the solidification front is assumed to repeat indefinitely the cycle of oscillation 1-2-3-4-1... in Fig. 5. In this cycle the transitions between steady-state branches, 1-2 and 3-4, are assumed to be quasi-instantaneous, and parts 2-3 and 4-1 of the cycle are assumed to correspond to slow quasi-steady-state changes in temperature along the steady-state branches. These changes are caused by the motion of the interface relative to the moving isotherm. In part 2-3 of the cycle the interface moves faster than the isotherm and therefore warms up, and, in part 4-1, it moves slower and therefore cools down. It should be noted that the assumed instability of the up-sloping

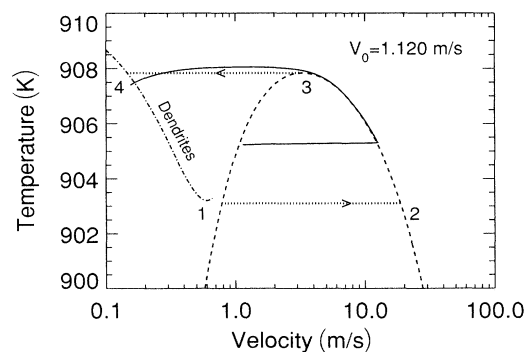


FIG. 5. The cycle 1-2-3-4-1 corresponds to the CGZK model [16], where the steady-state dendrite branch $T_{den}(V)$ and planar branch $T_{pl}(V)$ are represented by dash-dotted and dashed lines, respectively. The solid line corresponds to a cycle computed without latent-heat diffusion (FTA).

branch of the $T_{\text{pl}}(V)$ in the CGZK model is actually the same as the CS instability that occurs at $q = 0$ in the FTA (see Sec. III). In the FTA, the absolute stability limit of this instability is actually very close to the maximum of the $T_{\text{pl}}(V)$ curve as correctly assumed in the model. However, with LHD, its absolute stability limit occurs lower on the $T_{\text{pl}}(V)$ curve (at $V_c \simeq 1.42$ m/s).

Given the assumed cycle 1-2-3-4-1, it is then possible to calculate exactly the spacing of light and dark bands. This is done by differentiating Eq. (29) with respect to time, taking into account the fact that $T_i(t) = T_{\text{pl}}(V)$ on 2-3 [or $T_i(t) = T_{\text{den}}(V)$ on 4-1] where $V = d\xi(t)/dt$ is the instantaneous velocity of the interface. This differentiation yields at once the relation

$$\frac{dV}{dt} \frac{dT_{\text{pl}}(V)}{dV} = G(V - V_0)$$

valid on 2-3, and its analog

$$\frac{dV}{dt} \frac{dT_{\text{den}}(V)}{dV} = G(V - V_0)$$

on 4-1. Note that, in the FTA, $G^+ = G^- \equiv G$. By eliminating time via $dt = dz/V$ it is then easy to show that the total distance traveled by the interface on 2-3 (light band spacing) is given by

$$\lambda_{\text{light}} = \frac{1}{G} \int_{V_2}^{V_3} \frac{V dT_{\text{pl}}/dV}{V - V_0} dV \quad (57)$$

and the distance traveled on 4-1 (dark band spacing) by

$$\lambda_{\text{dark}} = \frac{1}{G} \int_{V_1}^{V_4} \frac{V dT_{\text{pl}}/dV}{V - V_0} dV. \quad (58)$$

2. Cycles computed using the frozen-temperature approximation

We have compared in Fig. 5 the cycle of oscillation of the CGZK model with the cycle calculated numerically using the FTA [i.e., the boundary integral formulation for the concentration field coupled to Eq. (28), which neglects LHD]. We also show in Fig. 6(a), for the same cycle, the time dependence of the interface velocity $V(t)$, the interface position $\xi(t)$ [recall that $\xi(t)$ is measured in a stationary frame], and the interfacial temperature change $\Delta T \equiv T_i(t) - T_i(0)$. We start the computed cycle from a point along the up-sloping part of the $T_{\text{pl}}(V)$ curve, about midway between 1 and 3. This choice is somewhat arbitrary and was made to render the comparison clearer (1 could have been chosen as well). The instability is triggered by choosing a starting velocity slightly higher than V_0 .

We first note that the part of the cycle analogous to 1-2 in the CGZK model occurs on a very short time scale marked by the abrupt change of velocity in Fig. 6(a). During this transition, the interfacial temperature changes very little, as shown by the horizontal jump between the unstable and stable branches of the $T_{\text{pl}}(V)$ curve in Fig. 5. Subsequently, the cycle of oscillation follows exactly the $T_{\text{pl}}(V)$ curve up to point 3, the temperature and velocity evolving slowly in time. This first part of the cycle (up to point 3) is nearly identical to that of the CGZK model.

The part of the computed cycle from 3 to 4 is nearly horizontal in Fig. 5 but does not occur instantaneously, as assumed in the CGZK model [Fig. 6(a)]. This part of the cycle can be roughly divided in two parts: the first from point 3 to the point of maximum temperature corresponding to $V = V_0$ (about midway between 3 and 4) and the second from the latter point to point 4. The first part occurs rapidly, as the initial horizontal velocity jump, and can be assumed to be quasi-instantaneous. The second part occurs much more slowly due to the fact that the interface velocity becomes much smaller (V varying from about 1 m/s to 0.1 m/s). Actually, it can be seen in Fig. 6(a) that the time spent on this section of the cycle (from midway between 3 and 4 to 4) is a significant portion of the total time spent on the entire cycle. The CGZK model therefore underestimates significantly the time spent in the second part of section 3-4 of the cycle.

This error in duration, however, does not alter significantly the analytical prediction [Eq. (57)] for the light band spacing λ_{light} . The reason for this is that, although the actual cycle spends a relatively long time along the second part of 3-4, the interface travels a relatively short distance during this part due to the fact that V is small.

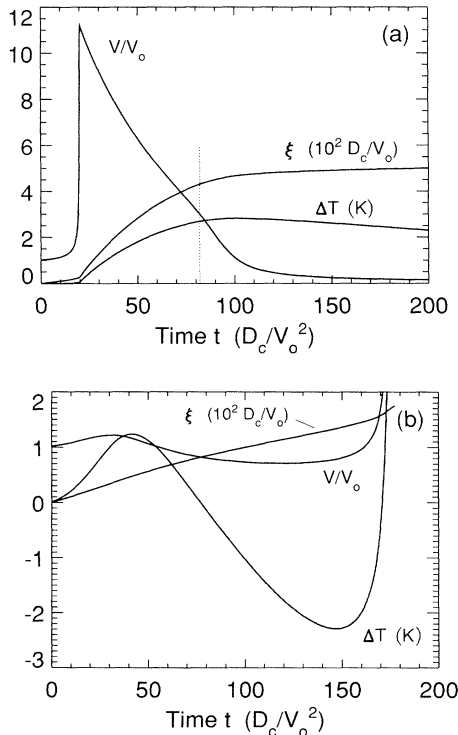


FIG. 6. Time variations of the velocity V , the interface position ξ in a stationary frame, and the interfacial temperature change $\Delta T \equiv T_i(t) - T_0$: (a) without LHD (FTA), and (b) with LHD, for the same initial conditions; (a) corresponds to cycle A, and (b) to cycle E, in Fig. 7. The dotted line in (a) marks the instant at which the cycle reaches the maximum of the $T_{\text{pl}}(V)$ curve (point 3 in Fig. 5).

Most of the interface displacement occurs on the down-sloping part of the $T_{pi}(V)$ curve where V is high. The CGZK model therefore only slightly underestimates the light band spacing as shown in Fig. 6(a).

To conclude this comparison, we note that we have only graphed in Fig. 5 the computed cycle up to point 4. Past this point, the planar interface continues to decelerate down to very small velocities (in the cm/s range) where it eventually starts accelerating again. However, this part of the cycle is unphysical since the breakdown of the planar interface caused by finite-wave-number instabilities occurs already in the last part of the 3-4 cycle. An indication of this breakdown is given by the linear stability spectrum of the planar interface, which develops a strong MS-type instability below about 0.5 m/s [Fig. 2(c)]. (This spectrum can only be used as a rough estimate here since the interface is actually not in the steady state during the deceleration cycle 3-4.) Finally, although our present numerics cannot be used to check the final portion 4-1 of the cycle, we expect it to be reasonably well described by the CGZK model together with the prediction of λ_{dark} .

C. Thermal effects

We now present the results of numerical simulations, which include LHD, and then explain why they turn out to be so large using the RTE derived in Sec. V.

1. The effect of latent-heat diffusion

To illustrate the effect of LHD we have compared in Fig. 7 the initial trajectories of the interface obtained using the same initial condition that was used in the previous comparison of Fig. 5, but with decreasing thermal diffusivities (in the order $A-E$). The two important trajectories are A , which corresponds to the FTA ($D_T \rightarrow \infty$) and is identical to the one displayed in Fig. 5, and E , which corresponds to the physical value of the thermal diffusivity for our model $D_T = 5.35 \times 10^{-5}$ m²/s. Trajec-

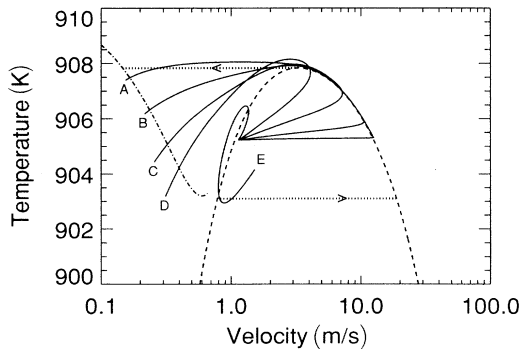


FIG. 7. Initial part of cycles computed with latent-heat diffusion and different D_T : (A) FTA ($D_T \rightarrow \infty$), (B) $D_T = 10^{-2}$ m²/s, (C) $D_T = 10^{-3}$ m²/s, (D) $D_T = 3 \times 10^{-4}$ m²/s, and (E) $D_T = 5.35 \times 10^{-5}$ m²/s. Cycles (B) and (C) correspond to values of D_T outside the physically realizable range, and are displayed to illustrate thermal effects.

tories $B-D$ correspond to cycles with decreasing values of D_T (10^{-2} , 10^{-3} , and 3×10^{-4} m²/s). Cycles A and E are also compared in Fig. 6.

The comparison of the two extremes A and E clearly shows that LHD has a dramatic effect on the trajectories of the planar interface in the $T-V$ plane. The physical origin of this effect can be understood qualitatively by noting that during its unsteady motion the interface produces an extra amount of latent heat proportional to $(L/c_p)[V(t) - V_0]$. The moving isotherm only carries out the heat generated by the interface moving exactly at V_0 . When the interface initially accelerates, as it leaves the unstable branch of the $T_{pi}(V)$ curve, it will produce an excess of latent heat that will tend to increase its temperature. On the contrary, after decelerating sufficiently it will eventually produce less latent heat than the amount which is carried away by the moving isotherm and its temperature will decrease. This accounts for the fact that the trajectories in the $T-V$ plane slope increasingly upwards during acceleration, and increasingly downwards during deceleration, as the effect of LHD is increased.

The above argument accounts “qualitatively” for the effect of latent-heat diffusion. However, it does not explain “quantitatively” why it is so large. We now show that a proper explanation of this quantitative role can be obtained using a short-time approximation of the RTE derived in Sec. V. We start by noting that the total interfacial temperature change $\Delta T \equiv T_i(t) - T_0$ caused by the unsteady motion of the interface can be written as the sum of two terms (see Fig. 8):

$$\Delta T = \Delta T_G + \Delta T_L. \quad (59)$$

The first term represents the temperature increase resulting from the advance (or retard) of the interface with respect to the moving isotherm

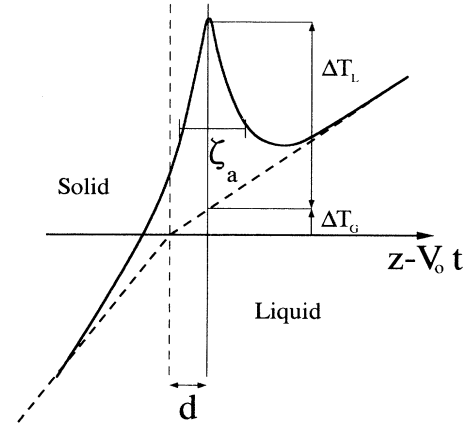


FIG. 8. Schematic drawing of the disturbance of the temperature profile following a rapid acceleration of the interface in the frame of the moving isotherm. The steady-state temperature profile and the interface, before and after the perturbation, are represented respectively by dashed and solid lines. ΔT_G and ΔT_L denote respectively the temperature changes resulting from motion of the interface in the temperature gradient and diffusion of excess latent heat. Note that the drawing is not to scale (in reality $\zeta_a \gg d$).

$$\Delta T_G = G^+ [\xi(t) - V_0 t]. \quad (60)$$

The second term ΔT_L represents the temperature increase resulting from the excess latent heat $(L/c_p)[V(t) - V_0]$ generated at the interface and is given by the second term on the RHS of Eq. (38):

$$\Delta T_L = \frac{L}{c_p} \int_0^t dt' \frac{V(t') - V_0}{\sqrt{4\pi D_T(t-t')}}. \quad (61)$$

To evaluate ΔT_G and ΔT_L in an unsteady growth situation one needs to know the time dependence of $V(t)$, which, in general, has to be calculated numerically by solving the coupled solutal-thermal problem. However, analytical estimates of the changes ΔT_G and ΔT_L , occurring during the initial acceleration period where the interface releases a large amount of excess latent heat, can be obtained by assuming that during this period the acceleration remains approximatively constant. It should be noted that an infinitesimal linear perturbation would lead to an initial exponential growth $\sim \Omega^2 \exp \Omega t$ of the acceleration, which is not relevant here. The short period where the acceleration is roughly constant already occurs in a nonlinear regime following a small but finite amplitude perturbation. Numerically, we have observed that following such a perturbation the interface acceleration is only very roughly constant. The above approximation should therefore only be interpreted to yield orders-of-magnitude estimates of ΔT_G and ΔT_L with the goal of understanding the quantitative role of LHD. Denoting by Γ_a the total duration of the acceleration period and substituting $V(t) = V_0 + \Delta V/\Gamma_a t$ into Eq. (60) [with $\xi(t) = \int_0^t V(t') dt'$] and Eq. (61), we obtain after performing elementary integrals

$$\Delta T_G = G^+ \bar{V} \Gamma_a, \quad \Delta T_L = \frac{L}{c_p} \sqrt{\frac{4}{9\pi}} \Delta V \sqrt{\frac{\Gamma_a}{D_T}},$$

where $\bar{V} \equiv (V_f + V_0)/2$ and $\Delta V \equiv V_f - V_0$ (V_0 and V_f denote, respectively, the initial and final velocities). For the interface acceleration to take place, the boundary layer of solute ahead of the interface needs to become thinner to accommodate a larger velocity. The acceleration therefore occurs on a time scale that is proportional to the diffusion time D_C/\bar{V}^2 . Substituting $\Gamma_a \sim D_C/\bar{V}^2$ into the above form for ΔT_G and ΔT_L we obtain the estimates

$$\Delta T_G \sim G^+ \frac{D_C}{\bar{V}}, \quad \Delta T_L \sim \frac{L}{c_p} \sqrt{Le}, \quad (62)$$

where we have dropped the numerical prefactor factor $\sqrt{4/9\pi}(\Delta V/\bar{V})$ of order unity. The quantitative importance of LHD can now be understood using the above relations. Using the typical value $\bar{V} = 1$ m/s together with $D_C = 1.7 \times 10^{-9}$ m²/s, $D_T = 53.5 \times 10^{-6}$ m²/s, $L/c_p = 349$ K, and the estimate $G^+ = 510^6$ K/m, we find $\Delta T_G \sim 10^{-2}$ K while $\Delta T_L \sim 1$ K. The conclusion is that $\Delta T_L \gg \Delta T_G$. The change in interface temperature due to LHD far exceeds the change due to interface motion in the temperature gradient.

The relation $\Delta T_L \gg \Delta T_G$ explains why in Fig. 7 the trajectories of the interface are so dramatically affected by LHD. Without this effect, the temperature remains nearly constant ($\Delta T_L = 0$) during its acceleration period and this is why the transition 1-2 appears to be nearly horizontal in the T - V plane (trajectory *A*). At the other extreme (trajectory *E*), LHD causes the interface to warm up considerably during its acceleration, and the reverse during its deceleration.

2. Cycles computed with latent-heat diffusion and thermal profiles

We show in Figs. 9(a)–9(d) cycles in the T - V plane for decreasing values of V_0 calculated using the exact integral formulation (Sec. VI A 1). Here, the initial transients are not shown and only the final cycles are displayed for clarity. The same cycles are also represented in Figs. 10(a)–10(d), where $V(t) = d\xi(t)/dt$ is plotted as a function of time. The time variations of composition on the solid and liquid sides of the interface are illustrated in Fig. 11. We also compare in Fig. 12 two cycles obtained for the same parameter values using (i) the exact formulation and (ii) the approximate reduced formulation based on the RTE (Sec. VI A 1), in order to verify the validity of the latter.

The character of oscillations changes rapidly [Figs. 9(a)–9(d) and 10(a)–10(d)] as the control parameter V_0 is decreased below the critical velocity $V_c = 1.42$ m/s corresponding to the onset of the $q = 0$ instability. For V_0 very close to V_c the oscillations first have an amplitude that increases as $\sqrt{V_c - V_0}$, and then evolve into large-amplitude relaxation-type oscillations for smaller values of V_0 . The relaxational character of these oscillations is clearly marked in the velocity versus time plots (Fig. 10) by the presence of sharp spikes, indicating abrupt velocity changes intercalated with slow quasi-steady-state changes.

Another important feature of the cycles is the occurrence of a classic period-doubling sequence of bifurcation to chaos with decreasing V_0 . Representatives of period 1-2-4 are shown respectively in Figs. 9(a)–9(c) and 10(a)–10(c). A typical chaotic state is shown in Figs. 9(d) and 10(d). It is interesting to note that the occurrence of period doubling and chaotic cycles seems to be intimately linked to the interplay of the thermal diffusion field with a bistable dynamics. In particular, in the context of explosive crystallization, where the dynamics of the planar interface is controlled by the thermal field via a local growth law $V = V(T_i)$, van Saarloos and Weeks had previously observed a similar period-doubling sequence of bifurcation [28]. In their case, the $V(T)$ curve possesses two branches (characteristic of bistable dynamics), which are analogous to the two branches of the steady state $T_{pl}(V)$ here. Thus, both banding and explosive crystallization have the common ingredient of being controlled in part by a long-range diffusion field (temperature) and some local bistable dynamics, which in one case (banding) is controlled by the concentration field, and the other

(explosive crystallization), by a local growth law.

To explore further the role of thermal effects we have displayed in Fig. 13 snapshots of the temperature profile, where the steady-state background has been subtracted (here $\Delta T \equiv T - T_{SS}$). The two instants, where the temperature reaches a maximum and a minimum value during the cycle, are shown. The large positive and negative spikes in the thermal profile are the result of the additional positive and negative heat flux $(L/c_p)[V(t) - V_0]$ generated at the interface and equal ΔT_L [Eq. (61)] at the interface ($z - \xi = 0$). The complete spatiotemporal evolution of the temperature profile for the same cycle is shown in Fig. 14.

As mentioned earlier, the scale $\zeta_T \sim \sqrt{D_T \Gamma_{osc}}$ characterizing the spatial extent of the thermal spikes is on the order of a few μm and therefore much larger than the average interface displacement ζ [Eq. (41)] which, here, is of the order of 50 nm. It should also be noted that the width of the thermal spike caused by the initial acceleration of the interface scales as $\zeta_a \sim \sqrt{D_T \Gamma_a} \sim \sqrt{l_C l_T}$, which is about one order of magnitude smaller than ζ_T . This narrower spike is then broadened diffusively during the slower quasi-steady-state portion of the cycle, which follows the $T_{pi}(V)$ curve.

D. Banding

1. Consequences of thermal effects

The small-amplitude oscillations [e.g., $V_0 = 1.393$ m/s in Figs. 9(a) and 10(a)] are characteristic of what is usually observed above threshold of a supercritical Hopf bifurcation. We would expect these oscillations to be modulated spatially by long-wavelength instabilities, which are suppressed by our numerics. Furthermore, these oscillations are too small in amplitude to cause the alternation of structure associated with banding to occur and are not particularly relevant here.

More relevant are the large-amplitude oscillations that occur at lower isotherm velocity. These carry the interface from a high-velocity regime (3–10 m/s), where finite q instabilities are suppressed, to a low velocity regime (0.5–1 m/s), where they are amplified and could lead to the formation of a transient cellular structure that would account for the presence of dark bands. Thus, an essential ingredient of the CGZK model—namely that banding results from large velocity changes that yield an alternation of structure—survives, at least qualitatively, when the effect of LHD is included. However, the nature of

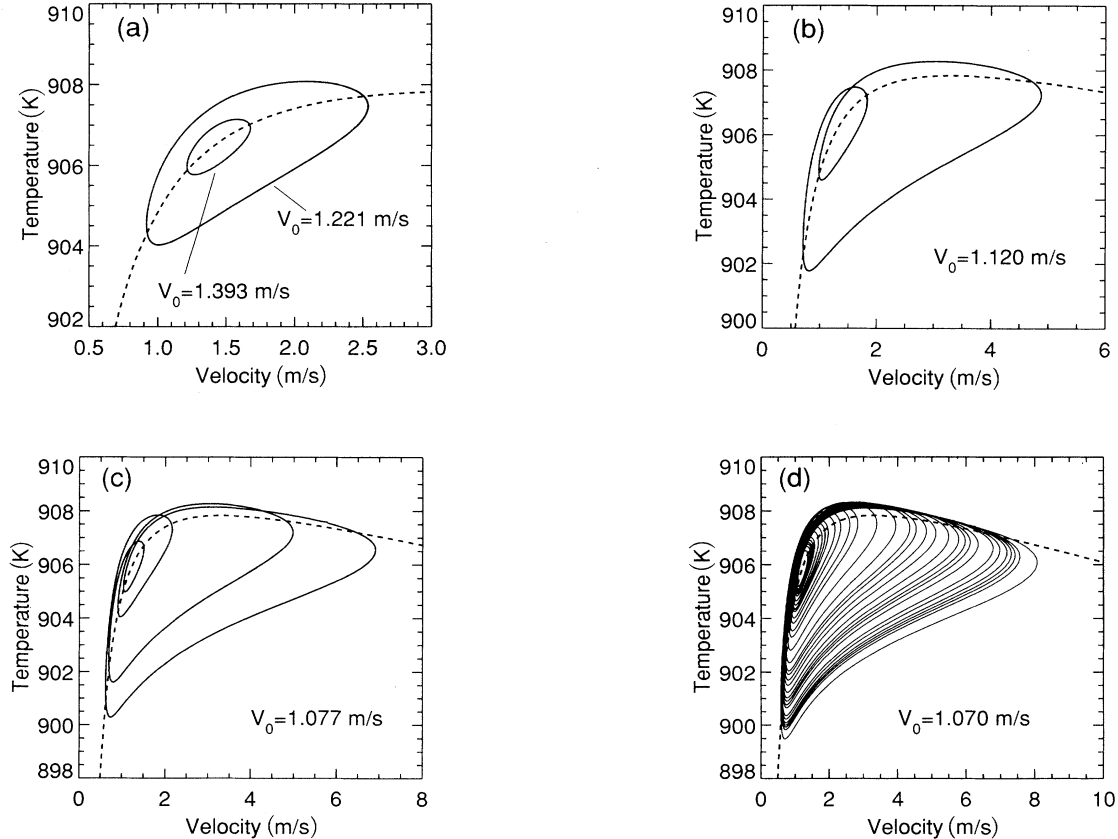


FIG. 9. Cycles computed with LHD represented in the T - V plane: (a) period-1, (b) period-2, (c) period-4, and (d) chaotic oscillations.

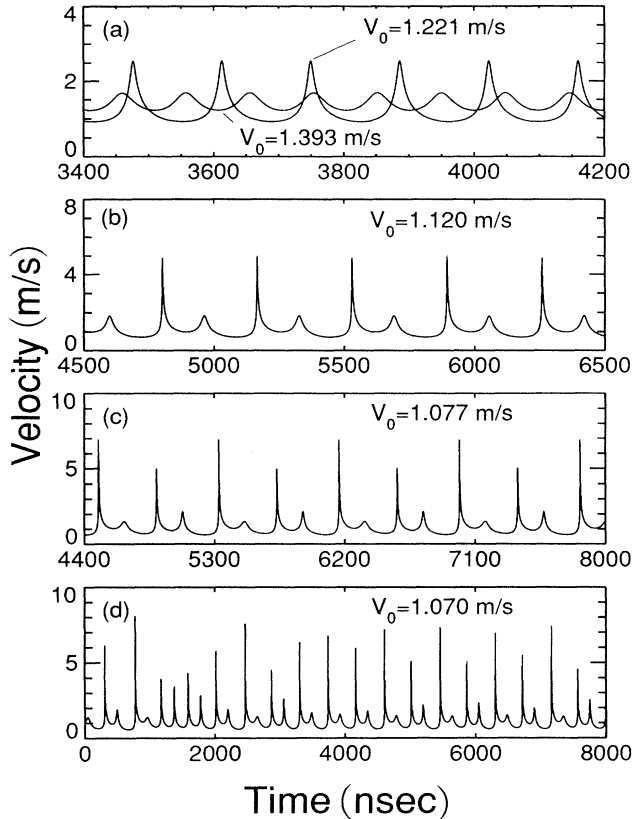


FIG. 10. Velocity V vs time for the same cycles shown in Fig. 9.

the cycles is dramatically altered by thermal effects as a direct consequence of the breakdown of the FTA. This alteration has two main consequences on the formation of the banded structure:

(i) *Band spacing.* The first is to change the physical mechanism controlling the band spacing.

Without LHD (FTA) we have found that computed cycles are to a large degree well approximated by the CGZK model. The model underestimates significantly the time spent on the decelerating portion of the cycle (3-4 in Fig.

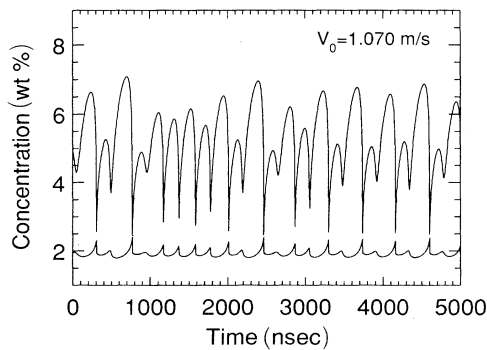


FIG. 11. Time variations of composition on the solid side (lower curve) and liquid side (higher curve) of the interface for the cycle of Figs. 9(d) and 10(d).

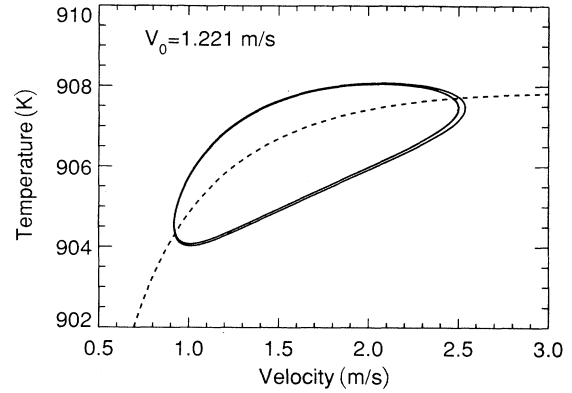


FIG. 12. Comparison of cycles computed using the exact integral formulation (outer loop) and the Fourier series representation of the reduced temperature equation (inner loop).

5), but this underestimation, in time, does not feed back significantly on the total interface displacement during the entire portion 1-2-3-4 of the cycle that controls the light band spacing. Consequently, in the FTA, the latter is well approximated by Eq. (57) and is inversely proportional to G . Although we cannot check here the last portion 4-1 of the cycle where the interface is nonplanar, we strongly expect that the total displacement on this part would also scale as G^{-1} since temperature changes can only occur via motion in the temperature gradient.

In contrast, with LHD, we find that the cycles themselves and, thus their average spacing $\bar{\lambda}$ (to be defined below), depend negligibly on the temperature gradient. As an illustration, we compare in Fig. 15 two cycles calculated respectively with $G^+ = 0$ and $G^+ = 5 \times 10^6$ K/m. The velocity is plotted as a function of interface position ξ , which allows us to read $\bar{\lambda}$ directly. When G^+ changes by over six orders of magnitude, $\bar{\lambda}$ changes by less than a few percent. This insensitivity is a direct consequence of the fact that the temperature changes during the cycle are controlled predominantly by LHD and that, as shown earlier, $\Delta T_L \gg \Delta T_G$. Instead, the cycles depend sensi-

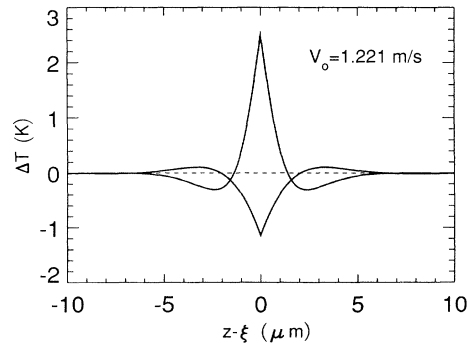


FIG. 13. Temperature profiles at the instants of maximum-temperature and minimum-temperature during the cycle. The background steady-state profile due to the moving isotherms has been subtracted to show the effect of LHD.

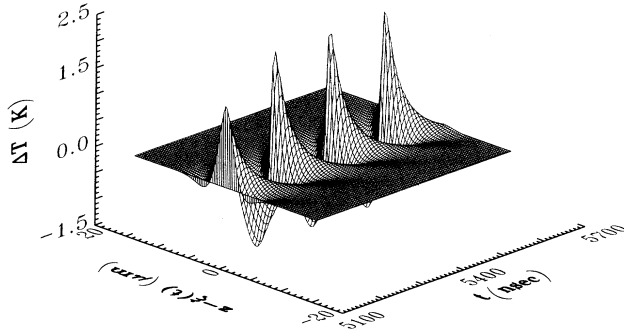


FIG. 14. Spatiotemporal variations of the temperature profile with a subtracted steady-state profile.

tively on the thermal diffusivity D_T , as shown previously in Fig. 7.

It would be useful to understand, on purely dimensional grounds, how the band spacing scales with the various parameters of the model. Without LHD, this scaling is simple. Namely, $\lambda \sim \Delta T/G$, where ΔT scales proportionally to the difference between the minimum temperature of the $T_{\text{den}}(V)$ curve and the maximum temperature of the $T_{\text{pl}}(V)$ curve ($\Delta T \sim T_3 - T_2$ in Fig. 5). With LHD, λ depends in a nontrivial way on the interplay of solute diffusion, which drives the acceleration and deceleration of the interface, and thermal diffusion, which drives the temperature changes. The simplest natural length scale to emerge from the interplay of solute and thermal diffusion is the width of the thermal spikes in the temperature profile created during the rapid acceleration periods, which, as noted before, scales as the geometric mean of l_C and l_T ,

$$\zeta_a \sim \sqrt{l_C l_T}.$$

We note that this scale has roughly the same order of magnitude as λ .

(ii) *Transverse structure and dark bands.* Although our present numerical calculation does not describe the formation of the nonplanar transverse structure, it provides a guide to interpret the origin and the nature of

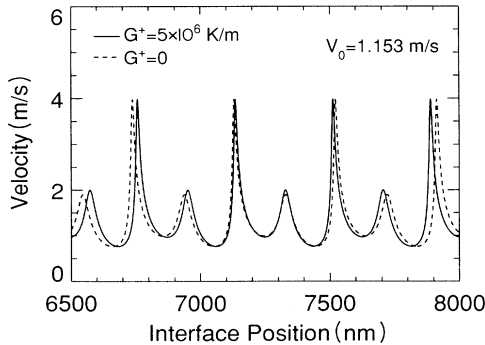


FIG. 15. Comparison of cycles computed with LHD for two vastly differing values of the temperature gradient G .

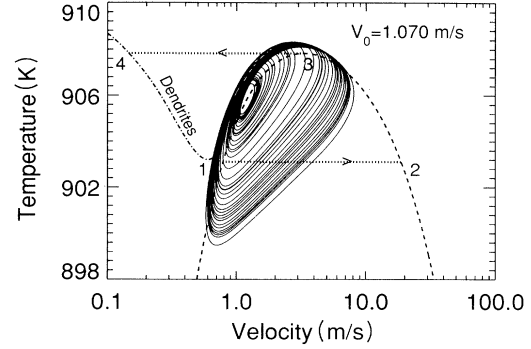


FIG. 16. Comparison of the CGZK cycle 1-2-3-4-1 and a large-amplitude cycle computed with LHD. This comparison is to be contrasted with that of Fig. 5.

this structure. For the purpose of the present discussion, we have compared in Fig. 16 with the CGZK cycle the largest-amplitude computed cycle that falls inside the chaotic regime. The most relevant feature to notice is that the computed cycles intersect the dendrite branch at its very end (near point 1) instead of point 4. Since the amplitude of the transverse cellular-dendritic structure (the cell depth) decreases from 4 to 1, we expect this structure to be of considerably smaller amplitude with thermal effects. This agrees qualitatively with the previous results of linear stability analysis, which indicate [Fig. 2(c)] that the crossover, from a small q dominated spectrum to a large q MS-type spectrum, occurs between 0.8 and 0.5 m/s, which corresponds roughly to the minimum velocity range reached during the cycle.

2. Comparison with experiment

A comparison of calculated and experimentally measured band spacings is given in Table III. As discussed in item (iii) at the beginning of Sec. VI, our present calculations cannot be used to predict λ_{light} and λ_{dark} independently. In a strict sense, they describe solute bands (see Fig. 11). However, they can be used to estimate the total spacing of banded structures dominated by light bands [Fig. 1(b)], assuming that this spacing is not greatly modified by the formation of a transient cellular structure during the low-velocity portion of the cycles.

The measured spacings in Table III correspond to the

TABLE III. Comparison of measured [8] and calculated spacings.

V_0 (m/s)	$\lambda_{\text{light}}/\lambda$	λ (nm)	V_0 (m/s)	$\bar{\lambda}$ (nm)
0.91	0.77	415	1.070	225
0.98	0.75	395	1.077	217
1.99	0.91	275	1.120	204
2.00	0.93	295	1.221	166
3.16	0.90	250	($V_0 > 1.42$)	No bands

values reported by Gremaud, Carrard, and Kurz for a 2 wt % Fe Al-Fe alloy over a velocity range corresponding to the one studied here. The ratio $\lambda_{\text{light}}/\lambda$ indicates the fraction of the banded structure occupied by light bands. The calculated spacings correspond to a value $\bar{\lambda}$ defined as the average spacing between successive velocity minima in the plot of velocity versus interface position [Figs. 17(a)–17(d)]. We use this definition instead of the total spatial period

$$\Lambda = \int_0^{\Gamma^{\text{osc}}} V(t) dt$$

because the latter diverges as the chaotic regime is approached (for period- 2^p cycles $\Lambda \sim 2^p \bar{\lambda}$).

Note also that $\bar{\lambda}$ should be considered a lower bound for the total band spacing since situations could arise where dark bands do not form at every velocity minima, but only at those where the amplitude of the transverse structure is sufficiently large to cause the precipitation of the impurity-rich (dark) phase.

The comparison of Table III shows that the calculated and measured spacings are in relatively good agreement given the uncertainties in the nonequilibrium coefficients v_d and v^* , and the fact that $\bar{\lambda}$ represents a lower bound. It should be emphasized that the present predictions are nearly independent of the value of G (Fig. 15). In contrast, in the CGZK model an upper limit of the temper-

ature gradient ($G^+ = 20 \times 10^6$ K/m) was used to match predicted and measured spacings [16]. The comparison also indicates that the predicted spacings are found to increase with decreasing V_0 as seen experimentally. One point of disagreement is the value of the upper velocity beyond which bands should not form, which here is equal to $V_c \simeq 1.42$ m/s, while experimentally bands are observed up to a maximum measurable velocity in the range 3–5 m/s.

An interesting question here, with regard to banding, is whether chaotic oscillations have a signature in the experimental micrographs. In particular, one could have expected such oscillations to lead to highly irregularly spaced bands. However, a close examination of Fig. 17(d) (which displays a chaotic cycle) reveals that the magnitudes of the velocity maxima are highly erratic but, in contrast, the velocity minima stay nearly regularly spaced. Since presumably only the latter are observable, we would not expect to see highly irregularly spaced bands. Finally, the fact that the erratic behavior of the velocity maxima does not feed back significantly on the spacing of velocity minima is a simple consequence of the fact that the interface spends only a short time of its cycle in a high-velocity regime (Fig. 10).

VII. CONCLUSIONS

In summary, we have investigated various aspects of interface dynamics in a model of rapid directional solidification that includes, in addition to solute diffusion, nonequilibrium effects and LHD. The main conclusions of this study with regards to banding are:

(1) A planar instability, which occurs below a critical velocity V_c less than the absolute stability limit V_{AS} , leads to large-amplitude relaxation oscillations of the solidification front. This instability has the same physical origin as the CS instability [11], namely solute trapping; a planar perturbation, which increases slightly the interface velocity, causes the interface to reject less solute and therefore to accelerate faster.

(2) The oscillation cycles are characterized by large velocity variations that carry successively the solidification front from a high-velocity regime where the planar interface is morphologically stable (up to some long-wavelength modulation) to a low-velocity regime where it is morphologically unstable and should form a cellular structure. We expect that the alternation of structure, characteristic of banding, results from such cycles. This expectation is strongly supported by the fact that the average cycle spacing $\bar{\lambda}$ falls, nearly independently of G , close to the measured [8] spacing of banded structures dominated by light microsegregation-free regions.

(3) The cycles obtained with the FTA used in recent studies of banding [14, 15] are described reasonably well by the CGZK model. This model contains, qualitatively, what seems to be the proper explanation of banding. However, quantitatively, the FTA-cycles are dramatically altered by LHD and do not provide a proper description of interface dynamics. This is reflected most strongly in the fact that, without LHD, the band spacing scales

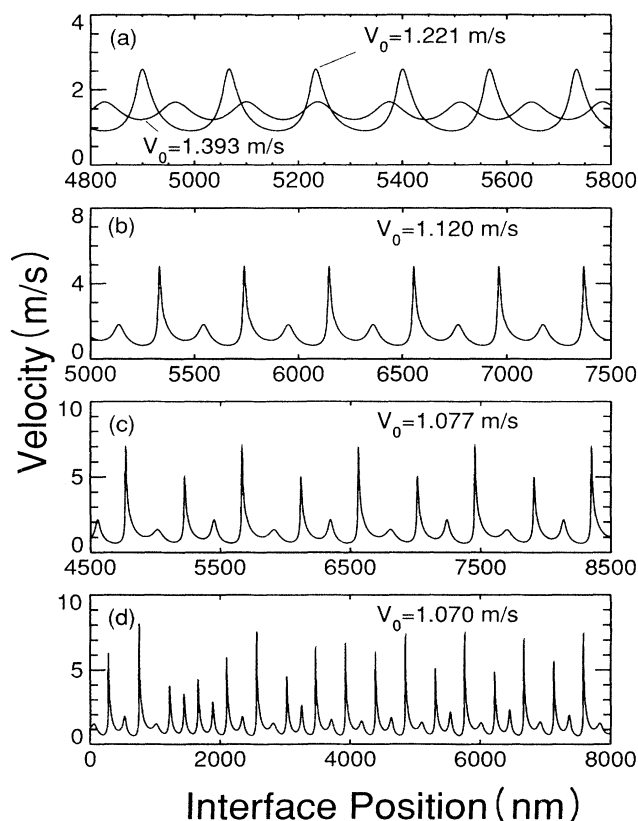


FIG. 17. Velocity V vs interface position ξ for the cycles corresponding to Figs. 9 and 10.

as G^{-1} , while, with LHD, it varies very little with G . LHD also leads to a dynamical behavior (period doubling, chaos, etc.) much richer than first anticipated. It should be noted, however, that finite-wave-number instabilities are very little affected by LHD and adequately described by the FTA [13].

(4) The effect of LHD can be understood in terms of a RTE, derived in the small Lewis number limit, which governs the change in interfacial temperature due to unsteady growth. This change is the sum of two parts:

$$\Delta T = \Delta T_G + \Delta T_L.$$

The first, $\Delta T_G \sim GD_C/V_0$, results from interface motion relative to the moving isotherm (FTA), and the second, $\Delta T_L \sim L/c_p\sqrt{D_C/D_T}$, results from LHD. For values of $G \sim 10^6$ – 10^7 K/m and $V_0 \sim$ m/s, characteristic of the RS experiment where banding is observed, $\Delta T_L \gg \Delta T_G$. Thus, despite the fact that $\sqrt{D_C/D_T}$ is small, the dynamics of the planar interface is influenced considerably more by LHD than by the temperature gradient.

An essential part of our understanding of banding that remains lacking, is an understanding of the role of long-wavelength instabilities and a description of the transverse cellular-dendritic structure expected to form during the low-velocity portion of the cycles. We expect this

structure to be of much smaller amplitude with LHD than without. However, to determine its amplitude and wavelength, and how it affects the overall cycle, a description of nonplanar dynamics is needed. This dynamics is considerably more difficult to study numerically than the planar dynamics (already nontrivial here), as it involves treating at the same time the unsteady motion and the deformation of the interface. In this paper, we have derived a new equation of motion for the thermal field (2D version of the RTE) which allows us to investigate this dynamics with considerably more efficiency. A study of nonplanar dynamics based on this equation is presently underway.

ACKNOWLEDGMENTS

This work grew out of discussions with Wilfried Kurz during the visit of one of us (A.K.) to the Swiss Federal Institute of Technology in Lausanne. We would like to thank him, together with Mike Aziz, Michel Carrard, Marco Gremaud, Rohit Trivedi, and Martin Zimmermann, for many fruitful exchanges. This research is supported by DOE Grant No. DE-FG02-92ER45471 and the Donors of the Petroleum Research Fund administered by ACS. This research has benefited from supercomputer time allocation at NERSC.

-
- [1] J. S. Langer, in *Chance and Matter*, Lectures on the Theory of Pattern Formation, Les Houches Summer School, Les Houches, 1986, edited by J. Souletie, J. Vannimenus, and R. Stora (North-Holland, New York, 1987), pp. 629–711.
 - [2] D. Kessler, J. Koplik, and H. Levine, *Adv. Phys.* **37**, 255 (1988).
 - [3] W. Kurz and R. Trivedi, *Acta Metall.* **38**, 1 (1990).
 - [4] G. V. S. Sastry and C. Suryanarayana, *Mater. Sci. Eng.* **47**, 193 (1981).
 - [5] These include Ag-Cu, Al-Cu, Al-Fe, Al-Pd, and Al-Zr alloys. A complete set of experimental references is given in Ref. [3].
 - [6] W. J. Boettinger, D. Shechtman, R. J. Schaefer, and F. S. Biancaniello, *Metall. Trans.* **15A**, 55 (1984).
 - [7] M. Zimmermann, M. Carrard, and W. Kurz, *Acta Metall.* **37**, 3305 (1989).
 - [8] Gremaud, M., Carrard, M., and Kurz, W., *Acta Metall.* **39**, 1431 (1991).
 - [9] D. J. Thoma, T. K. Glasgow, S. N. Tewari, J. H. Perepezko, and N. Jayaraman, *Mater. Sci. Eng.* **98**, 89 (1988).
 - [10] W. W. Mullins and R. F. Sekerka, *J. Appl. Phys.* **35**, 444 (1964).
 - [11] S. R. Coriell and R. F. Sekerka, *J. Cryst. Growth* **61**, 499 (1983).
 - [12] A. Karma and A. Sarkissian, *Phys. Rev. Lett.* **27**, 2616 (1992).
 - [13] G. J. Merchant and S. H. Davis, *Acta Metall.* **38**, 2683 (1990).
 - [14] G. J. Merchant, R. J. Braun, K. Brattkus, and S. H. Davis, *SIAM J. Appl. Math.* (to be published).
 - [15] K. Brattkus and D. I. Meiron, *SIAM J. Appl. Math.* (to be published).
 - [16] M. Carrard, M. Gremaud, M. Zimmermann, and W. Kurz, *Acta Metall.* **40**, 983 (1992).
 - [17] M. J. Aziz, in *Undercooled Alloy Phases*, edited by E. W. Collings and C. C. Koch (TMS-AIME, Warrendale, PA, 1987).
 - [18] J. S. Langer, *Rev. Mod. Phys.* **52**, 1 (1980).
 - [19] M. J. Aziz and T. Kaplan, *Acta Metall.* **36**, 2335 (1988).
 - [20] W. J. Boettinger and S. R. Coriell, in *Science and Technology of the Undercooled Melt*, edited by P. R. Sahm, H. Jones, and C. M. Adam (NATO, Greenbelt, MD, 1986).
 - [21] M. J. Aziz, J. Y. Tsao, M. O. Thomson, P. S. Peercy, and C. W. White, *Phys. Rev. Lett.* **56**, 2489 (1986).
 - [22] K. A. Jackson, G. H. Gilmer, and H. J. Leamy, in *Laser and Electron Beam Processing of Materials*, edited by C. W. White and P. S. Peercy (Academic, New York, 1980).
 - [23] J. C. Baker and J. W. Cahn, in *Solidification* (American Society for Metals, Metals Park, OH, 1971), p. 23.
 - [24] R. Trivedi and W. Kurz, *Acta Metall.* **34**, 1663 (1986).
 - [25] J. S. Langer and L. A. Turski, *Acta Metall.* **25**, 1113 (1977).
 - [26] G. Barton, *Elements of Green's Functions and Propagation* (Oxford University Press, New York, 1989).
 - [27] J. Strain, *SIAM J. Sci. Stat. Comput.* (to be published).
 - [28] W. van Saarloos and J. D. Weeks, *Phys. Rev. Lett.* **51**, 1046 (1983).

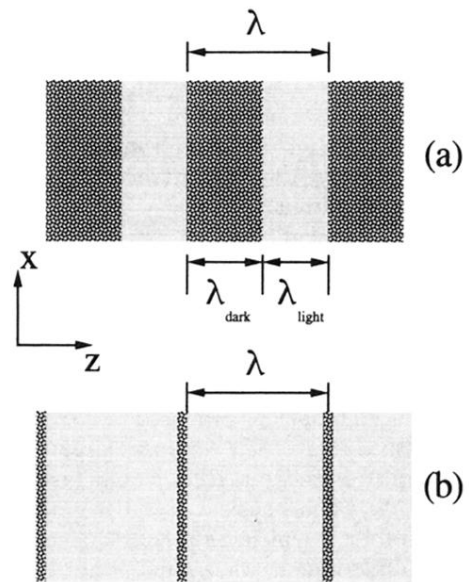


FIG. 1. Schematic drawing of the banded structure. The z and x axes are respectively parallel to the growth direction and to the solidification front.

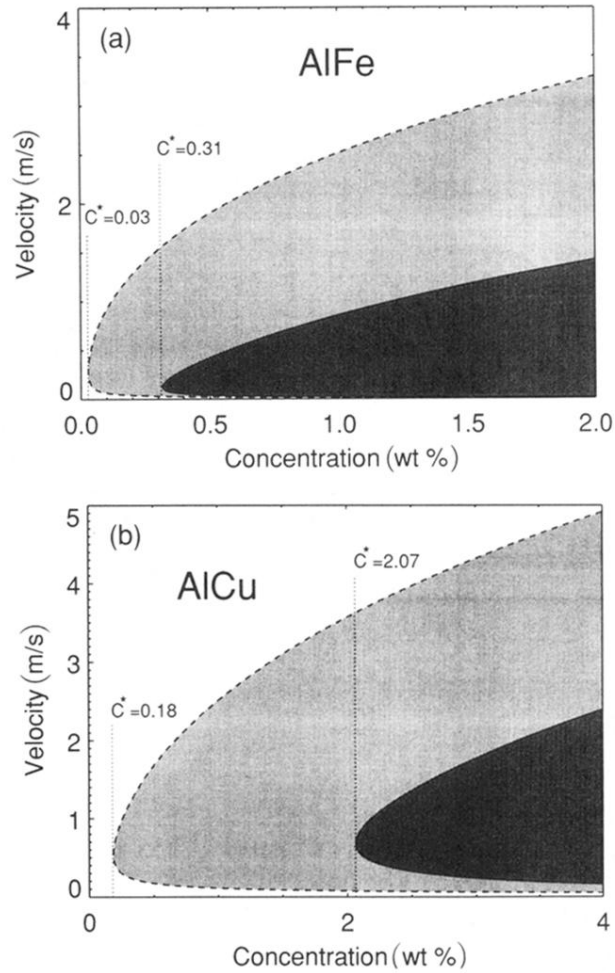


FIG. 4. Neutral stability boundaries of the $q = 0$ planar instability: (a) Al-Fe, and (b) Al-Cu. The light and dark shaded regions correspond to unstable regions, as predicted respectively by the FTAS [13] (light) and FS (dark). The upper neutral stability boundary of the planar instability for the FTAS also corresponds to the absolute stability limit of the FS. C^* indicates the lower critical composition below which banding should not occur. Note that C^* is underestimated by the FTAS.